Machine learning-based detection of weather fronts and associated extreme precipitation

Katherine Dagon[1,1], John E. Truesdale[2,2], James C. Biard[3,3], Kenneth E Kunkel[4,4], Gerald A. Meehl[2,2], and Maria J. Molina[1,1]

[1]National Center for Atmospheric Research
[2]National Center for Atmospheric Research (UCAR)
[3]ClimateAi
[4]North Carolina State University

November 30, 2022

Abstract

Extreme precipitation events, including those associated with weather fronts, have wide-ranging impacts across the world. Machine learning-based detection algorithms can help with the automated classification of the synoptic-scale weather features that produce extreme precipitation events, such as fronts. Here we use a deep learning algorithm to identify weather fronts in high resolution Community Earth System Model (CESM) simulations over North America, and validate the results using observational and reanalysis products. We further compare results between CESM simulations using present-day and future climate forcing, to study how fronts and extreme precipitation might change with climate change. We find that detected front frequencies in CESM have seasonally varying spatial patterns and responses to climate change, and are found to be associated with modeled changes in large scale circulation such as the jet stream. We also associate the detected fronts with extreme precipitation, and find that extreme precipitation associated with fronts mostly decreases with climate change, with some seasonal and regional differences. These changes appear to be largely driven by changes in the frequency of fronts, especially in Northern Hemisphere winter, demonstrating that extreme precipitation has seasonally varying sources and mechanisms that will continue to evolve with climate change.

Machine learning-based detection of weather fronts and associated extreme precipitation in historical and future climates

Katherine Dagon[1], John Truesdale[1], James C. Biard[2], Kenneth E. Kunkel[3], Gerald A. Meehl[1], and Maria J. Molina[1]

[1]National Center for Atmospheric Research, Boulder, CO, USA
[2]ClimateAi, San Francisco, CA, USA
[3]North Carolina Institute for Climate Studies, North Carolina State University, Asheville, NC, USA

Key Points:

- A deep learning algorithm is applied to detect weather fronts in climate model simulations over the contiguous United States
- Detected fronts have seasonally varying spatial patterns of front frequencies and responses to climate change
- Total and extreme precipitation associated with fronts mostly decreases with climate change, largely driven by changes in fronts

Corresponding author: Katherine Dagon, `kdagon@ucar.edu`

Abstract

Extreme precipitation events, including those associated with weather fronts, have wide-ranging impacts across the world. Here we use a deep learning algorithm to identify weather fronts in high resolution Community Earth System Model (CESM) simulations over the contiguous United States (CONUS), and evaluate the results using observational and reanalysis products. We further compare results between CESM simulations using present-day and future climate forcing, to study how these features might change with climate change. We find that detected front frequencies in CESM have seasonally varying spatial patterns and responses to climate change and are found to be associated with modeled changes in large scale circulation such as the jet stream. We also associate the detected fronts with precipitation and find that total and extreme frontal precipitation mostly decreases with climate change, with some seasonal and regional differences. Decreases in Northern Hemisphere summer frontal precipitation are largely driven by changes in the frequency of different front types, especially cold and stationary fronts. On the other hand, Northern Hemisphere winter exhibits some regional increases in frontal precipitation that are largely driven by changes in frontal precipitation intensity. While CONUS mean and extreme precipitation generally increase during all seasons in these climate change simulations, the likelihood of frontal extreme precipitation decreases, demonstrating that extreme precipitation has seasonally varying sources and mechanisms that will continue to evolve with climate change.

Plain Language Summary

Extreme precipitation can have devastating impacts on communities and ecosystems around the world. One source of extreme precipitation is weather fronts, or the boundaries between different types of air masses which can also give rise to high winds, rain, and thunderstorms. Machine learning can be used to automatically detect weather fronts in observations and model simulations. In this work, we use a machine learning algorithm to detect weather fronts in a climate model, and compare present day fronts with those detected in simulations with future climate change. We also compare detected fronts with total and extreme precipitation, to better understand sources of extreme precipitation and how they are changing with climate change.

1 Introduction

Extreme precipitation has significant consequences and impacts on communities and ecosystems and is expected to increase in intensity with climate change (Allen & Ingram, 2002; Tebaldi et al., 2006). Extreme precipitation also originates from many different sources and it is important to understand these sources, their associated mechanisms, and how they might change in a warming climate (Barlow et al., 2019). Weather fronts are synoptic-scale features defined as the interface between two air masses of different density and/or thermal characteristics (*American Meteorological Society Glossary of Meteorology: Front*, n.d.), and have been linked with other precipitation-generating features like extratropical cyclones (Kunkel & Champion, 2019). In the midlatitudes, extreme precipitation is often associated with weather fronts, with recent work finding 50-70% of extreme precipitation events over North America linked to fronts (Catto & Pfahl, 2013; Kunkel et al., 2012). Cold fronts have been shown to produce a significant amount of rainfall and particularly intense rainfall in areas of southern Australia (Pepler et al., 2020) and South Africa (Burls et al., 2019). Schemm et al. (2017) found an increase in the frequency of extremely strong fronts over Europe due to increases in atmospheric humidity, using historical reanalysis data. Blázquez and Solman (2019) found a similar result using climate model simulations, where Southern Hemisphere frontal precipitation largely increased with climate change due to increases in specific humidity. Hénin et al. (2019) found the opposite response in the Gulf Stream region, where frontal precipitation decreased due to changes in cold fronts. These studies point to a need for analyzing regional and seasonal changes in fronts of different types as an important component to understanding how total and extreme precipitation, and their associated impacts, might change in the future.

Previous work has developed objective methods to identify atmospheric fronts in weather and climate data by calculating the gradient of various surface fields and examining where the gradient is changing quickly in space and time. For example, Kunkel et al. (2012) used temperature gradients, wind shifts, local minima in the pressure fields, and changes in the dewpoint temperatures to identify fronts in weather station data. Hewson (1998) proposed using wet-bulb potential temperature to diagnose fronts, and this method was utilized in Berry, Reeder, and Jakob (2011) to identify fronts in the European Centre for Medium range Weather forecasts (ECMWF) ERA-40 reanalysis, and by Catto et al. (2012) in a similar approach with ERA-Interim. These studies further examined front speed to distinguish between different types of fronts. Simmonds et al. (2012) found the meridional component of wind to be the best field for identifying and tracking extratropical fronts in the Southern Hemisphere. Schemm et al. (2015) compared both temperature- and wind-based methods for detecting fronts and found that the thermal method was better suited to identify fronts in strong baroclinic settings such as low pressure systems in Northern midlatitudes. However, for areas outside the midlatitudes, the wind-based method was preferred to identify fronts, such as for cases associated with strong wind shear. Hope et al. (2014) compared five different automated frontal identification methods in reanalysis data over Western Australia, and discussed trade-offs and ideal use cases for thermal, wind, and statistical methods such as self-organizing maps and pattern matching. Parfitt et al. (2017) introduced a front detection method that combined thermal and non-thermal variables, which has the advantages of being robust and easy to calculate. Bitsa et al. (2021) also combined dynamic and thermodynamic criteria in cold front detection over the Mediterranean, and found improved performance relative to a wind-only scheme. The subjective choices that go into defining an automated front detection method were discussed further in Thomas and Schultz (2019b), including advantages of disadvantages of different quantities used in frontal analysis and mathematical functions used to define fronts. Thomas and Schultz (2019a) discuss how climatological analyses may be additionally impacted by the choice of atmospheric level at which to analyze fronts (e.g., surface or 850 hPa) and the particular thresholds used to define a front.

Machine learning and deep learning have provided an additional approach for automated front detection, further increasing the efficiency beyond hand-labeled efforts and allowing for the use of multiple fields in the detection process (Biard & Kunkel, 2019). Wong et al. (2008) used pattern recognition via a genetic algorithm and achieved high precision and efficiency in identifying weather systems, including fronts, with a variety of meteorological fields. Lagerquist et al. (2019) leveraged a deep learning approach via a convolutional neural network (CNN) to detect warm and cold fronts, and found that the CNN outperformed a human-labeled analysis on the basis of probability of detection and success ratio metrics. Biard and Kunkel (2019) also developed a CNN-based deep learning algorithm (DL-FRONT) for identifying weather fronts, and in validation testing the CNN correctly predicted the “front / no front” labels for 90% of 1° grid cells over North America. Front crossing rate climatologies calculated using the CNN predictions agreed well with those calculated using the Coded Surface Bulletin label data, with a Pearson’s correlation coefficient better than 0.94 for the grid cells within a rectangular region of interest centered over the contiguous United States.

While several previous studies have applied front detection methods to observations and reanalysis data (e.g., Berry, Reeder, & Jakob, 2011; Catto et al., 2012; Soster & Parfitt, 2022), few have utilized global high resolution coupled climate models for this purpose. Catto et al. (2013) identified fronts in the Australian Community Climate and Earth System Simulator (ACCESS) atmosphere model, though the simulations were not coupled and run at a lower horizontal resolution of 150 km. Catto et al. (2014) expanded this analysis to the Coupled Model Intercomparison Project, version 5 (CMIP5) models for current and future climate conditions and found consistent results with the single atmosphere-only model of Catto et al. (2013). The horizontal resolution of these models varied, though none of the models had a resolution finer than 0.75°. Catto, Jakob, and Nicholls (2015) further evaluated winter frontal precipitation in the same models and found good representation of front frequencies with some biases in total frontal precipitation, relating to compensating errors in the models. Leung et al. (2022) applied the method of Catto, Jakob, and Nicholls (2015) to the Coupled Model Intercomparison Project Phase 6 (CMIP6) models with a typical horizontal resolution of 1° and found a similar compensation of bias terms from the frequency and intensity of frontal precipitation. Blázquez and Solman (2019) focused on changes in wintertime frontal precipitation in the Southern Hemisphere in a selection of CMIP5 models with atmospheric resolution no finer than 1.4°, and found humidity-driven increases in fronts over most of the region. Regionally varying changes in precipitation were largely consistent with changes in fronts over mid and high latitudes, confirming the results of Utsumi et al. (2016) which showed that precipitation from extratropical cyclones including fronts increased poleward of storm tracks in future projections with a similar set of CMIP5 models.

In this paper, we use the deep learning-based detection algorithm from Biard and Kunkel (2019) to identify weather fronts over the contiguous United States in high resolution (0.25°) Community Earth System Model (CESM) simulations. We evaluate the CESM results by comparing seasonal front frequencies with detected fronts in observational and reanalysis products. We then compare detected fronts in different modeled climates to study the impact of climate change on weather fronts. Here we build on previous literature analyzing observed historical trends in fronts by leveraging automated front detection and climate model simulations to understand the longer term projected climate changes (e.g., late 21st century). We further associate the detected fronts with total and extreme precipitation, studying responses across seasons and front types, to understand how climate change impacts the intersection of synoptic-scale features with extreme events.

2 Data and Methods

2.1 DL-FRONT Detection Algorithm

The DL-FRONT algorithm from Biard and Kunkel (2019) is based on a CNN architecture, and developed using supervised learning where labeled fronts were used to train the CNN based on a set of meteorological fields as inputs. As a class of deep learning models (Krizhevsky et al., 2012; LeCun et al., 2015), CNNs have demonstrated success in detection of weather and climate features (e.g., Liu et al., 2016; Lagerquist et al., 2019; Molina et al., 2021). Increases in computational power to train deep learning models such as CNNs, combined with techniques to combat overfitting and improve stability, have increased the usage of CNNs for climate and meteorological applications. The deep and flexible architectures of CNNs allow them to learn broad features from data via visual pattern recognition. Compared to traditional gradient-based approaches for identifying fronts which use rules imposed by humans, CNNs aim to replicate how humans visually identify fronts by automatically learning from data. CNNs utilize multiple layers to transform the input into abstract representations of the original data, which is often spatially gridded. DL-FRONT uses five different types of layers: convolutional layers, rectified linear unit (ReLU) layers, dropout layers, zero-padding layers, and a softmax layer. These different layer types have specific purposes designed to process and learn features from the data. Convolutional layers use spatial filters to convolve the input data grid to produce an output data grid, consisting of feature maps. The ReLU and softmax layers are activation layers which apply nonlinear functions to the feature maps in order to learn nonlinear relationships. Dropout layers randomly zero out a fraction of the feature maps to prevent overfitting the data during training. Zero-padding layers counter the spatial shrinking from convolutional layers by padding the output data grid with additional zero-valued rows and columns. DL-FRONT was trained by optimizing network weights and biases to minimize the difference, as measured by a loss function, between the labeled fronts and the network-predicted fronts based on meteorological input data. The meteorological fields used as inputs to train DL-FRONT were 3-hourly instantaneous 2-meter air temperature, 2-meter specific humidity, air pressure reduced to mean sea level, the 10-meter east-west (u) component of wind velocity, and the 10-meter north-south (v) component of wind velocity. All input fields were taken from the Modern-Era Retrospective Analysis for Research and Applications, Version 2 (MERRA-2) (Gelaro et al., 2017). Input fields were sampled at 1° resolution over a specific North American domain (10-77°N, 171-31°W) for the years 2003-2015. The output labels were taken from the National Weather Service (NWS) Coded Surface Bulletin (CSB) dataset (National Weather Service, 2019; Biard, 2019). This dataset includes front types and locations identified by NWS meteorologists from 2003-2015. 87.42% of cells were labeled as "not front" and 12.58% of cells were labeled as "front" by the thickened CSB polygons, pointing to some asymmetry in this set of labels. Of those 12.58% labeled as "front", 56.12% were predicted as front by DL-FRONT and 43.88% were not. We refer the reader to Biard and Kunkel (2019) for more specific details on the DL-FRONT CNN architecture and training process.

2.2 Model Simulations

We utilize high resolution CESM version 1.3 (CESM1.3) (Meehl et al., 2019) simulations of present-day and future climate change to detect fronts and associated total and extreme precipitation. Higher resolution CESM offers more realistic simulated weather and climate, including a better representation of orography and storms, which is important for the representation of extreme precipitation in the model (Wehner et al., 2014). CESM1.3 includes the CAM5 atmospheric model (Park et al., 2014) with a spectral element dynamical core (Dennis et al., 2012) and a horizontal resolution of 0.25° with 30 vertical levels in the atmosphere. The other model components include the Community Ice Code Version 4 for sea ice (CICE4) (Hunke & Lipscomb, 2008), the Parallel Ocean Program Version 2 for the ocean (POP2) with a horizontal resolution of 1° and higher resolution in the equatorial tropics (Smith et al., 2010; Danabasoglu et al., 2012), and the Community Land Model Version 4 for the land (CLM4) (Lawrence et al., 2011) with the River Transport Model Version 1.

To match the years used to train DL-FRONT, we sample a CESM1.3 historical climate simulation from 2000-2005 that is forced by time varying natural and anthropogenic forcings (Meehl et al., 2019). To extend the years in our historical sample, we also use a CESM1.3 simulation with Representative Concentration Pathway 2.6 (RCP2.6) forcing from 2006-2015. The RCP2.6 simulation serves as the continuation of the historical CESM1.3 simulation, with a relatively low increase of anthropogenic forcing during the 21st century (van Vuuren et al., 2011), though the forcing and corresponding climate response across all the RCP scenarios is very similar during this time period early in the century (Meehl et al., 2013). We further sample the years 2086-2100 from a simulation with Representative Concentration Pathway 8.5 (RCP8.5) with the same CESM1.3 configuration, to investigate the response of climate change at the end of the 21st century in a simulation with a high forcing level (Riahi et al., 2011).

We post-process the CESM simulation output to prepare it for input to DL-FRONT using the following steps: (i) we resample the higher horizontal resolution of CESM from 0.25° to 1° to match the resolution of DL-FRONT using bilinear interpolation, (ii) we subset the spatial area to match the North American domain of Biard and Kunkel (2019), and (iii) prepare yearly input files for each variable. We strive to match the input variables as closely as possible to Biard and Kunkel (2019) given the simulation output availability and the need for high-temporal resolution fields. The following CESM output fields are available at 3-hourly instantaneous resolution: surface temperature (TS), sea level pressure (PSL), lowest model level zonal wind (UBOT), and lowest model level meridional wind (VBOT). With the exception of PSL, these are not the same exact fields used in the training of DL-FRONT but they are very close substitutions. 2-meter specific humidity was not available at 3-hourly instantaneous resolution for the CESM historical or RCP8.5 simulations, but full field 3D specific humidity (Q) was available at 3-hourly average resolution. Thus, we use the lowest model level specific humidity (QBOT) as a replacement for 2-meter specific humidity. For the RCP2.6 simulation, humidity was not available at 3-hourly temporal resolution, so here we use 6-hourly total vertically integrated precipitable water (TMQ) interpolated to 3-hourly resolution. We also calculate and update the scales and offset values needed for DL-FRONT specifically for each analysis period and dataset (i.e., unique scales and offset values were used for the input variables from CESM historical, CESM RCP2.6, CESM RCP8.5, and MERRA-2 data).

2.3 Associating Total and Extreme Precipitation with Fronts

To investigate the association between total and extreme precipitation with detected fronts in the model, we analyze the precipitation output from the same CESM simulations that are used to detect fronts. Since precipitation was not an input field used to detect fronts, we can treat these metrics as somewhat independent (though precipitation will be influenced by other fields used to detect fronts, such as humidity and pressure). We utilize the 3-hourly average precipitation rate (PRECT) from the CESM simulations to compute total and extreme precipitation. Total precipitation is calculated on a seasonal basis for each gridpoint over the contiguous United States (CONUS; 26-50°N, 125-68°W) by summing over time. We then calculate the total precipitation associated with a front by summing over time the precipitation where there is also a detected front in the same gridpoint at the same time. Here we consider only gridpoints labeled as front by DL-FRONT, rather than an expanded area of influence (e.g., Catto & Pfahl, 2013). The fraction of total precipitation associated with a front is computed by dividing total frontal precipitation by total precipitation, with separate calculations for each season and front type. Changes are calculated comparing 15-year climatologies of the CESM historical simulation (2000-2014) with the CESM RCP8.5 simulation (2086-2100). We further decompose the changes in total frontal precipitation into frequency and intensity terms, following similar approaches in Utsumi et al. (2016) and Pepler et al. (2021). The change in total precipitation associated with a front ΔP_F can be represented by the sum of three terms: the change due to frequency change, the change due to intensity change, and a covariation term (Equation 1). The frequency term is the product of the change in front frequency Δn_F and the mean precipitation intensity per associated front in the historical climate I_F, the intensity term is the product of the front frequency in the historical climate n_F and the change in mean precipitation intensity per associated front ΔI_F, and the covariation term is the product of the changes Δn_F and ΔI_F. The covariation term is small compared to the other two terms, thus we only include the frequency and intensity terms in our analysis.

$$\Delta P_F = \Delta n_F I_F + n_F \Delta I_F + \Delta n_F \Delta I_F \tag{1}$$

We calculate extreme precipitation based on the 90th percentile precipitation over land from the CESM historical simulation. While numerous definitions exist for extreme precipitation (Alexander et al., 2019; Schär et al., 2016), we choose the 90th percentile to include sufficiently intense precipitation events that provide adequate samples that could potentially be excluded using a more stringent index. More specifically, we calculate 90th percentile precipitation independently for each gridpoint and individually for each season, and use this location-based threshold to select where precipitation exceeds the 90th percentile value for that location and season. As we are interested in evaluating changes in fronts and extreme precipitation relative to present day climate, we use the same baseline period from the CESM historical simulation (2000-2014) to define extreme precipitation in both the historical and RCP8.5 simulations, following the approaches used in similar studies (e.g., Tebaldi et al., 2006; Sillmann, Kharin, Zwiers, et al., 2013; Utsumi et al., 2016). We calculate frontal extreme precipitation by selecting the extreme precipitation points that also include a detected front in the same gridpoint at the same time. As with the total frontal precipitation, we consider only gridpoints labeled as front by DL-FRONT. We use the probability ratio (PR) metric (Fischer & Knutti, 2015) to summarize frontal extreme precipitation as a ratio of the frequencies of occurrence (Equation 2). More specifically, this metric compares the conditional probability of frontal extreme precipitation ($N_P|F/N_F$) to the climatological probability of extreme precipitation (N_P/N), where N is the number of time steps, N_P is the number of time steps with extreme precipitation, N_F is the number of time steps with fronts, and $N_P|F$ is the number of extreme precipitation time steps associated with fronts. In other words, the PR is the factor by which the probability of frontal extreme precipitation is more likely to occur, with separate calculations for each season within the CESM historical and RCP8.5 simulations.

$$PR = \frac{N_P|F/N_F}{N_P/N} \tag{2}$$

3 Model Evaluation

To evaluate the detected fronts in CESM, we apply the trained DL-FRONT model to post-processed CESM historical simulation output (2000-2015). The output of DL-FRONT produces spatial grids that represent the likelihood of the presence of a front, separated into 5 different categories: cold (which marks the leading edge of an advancing colder air mass), warm (which marks the leading edge of a warmer air mass advancing partly due to colder air retreating), stationary (which marks a boundary between cold and warm air masses that have stopped moving), occluded (which is generally where a cold air mass overtakes a slower moving warm air mass), and none. We further use post-processing tools developed by Biard and Kunkel (2019) to produce "one-hot" encoded versions of the front probabilities and polylines outlining front boundary locations. These files are then used to calculate monthly, seasonal, and annual front crossing rates (the frequency of fronts passing over a particular location) as well as monthly and seasonal front crossing rate climatologies and anomalies (Biard & Kunkel, 2019). Seasonal climatologies are calculated over four 3-month periods: December-January-February (DJF), March-April-May (MAM), June-July-August (JJA), and September-October-November (SON). The resulting CESM seasonal front crossing rate climatologies are delineated by front type and averaged over CONUS, as shown in Figure S1. Comparing panels a) and b) of Figure S1, we see that the transition to RCP2.6 forcing in year 2006 does not appear to have a significant effect on the CESM front crossing rate climatology. In addition, using TMQ instead of QBOT from the RCP2.6 simulation (due to data availability constraints) does not appear to significantly change the resulting climatology. There is a slight decrease in front crossing rates evident in JJA, but is within the standard deviation across years. The overall climatology for the CESM historical simulations (2000-2015) is shown in panel c) of Figure S1. Cold and stationary fronts are more frequent than warm and occluded fronts across all seasons.

We compare the CESM historical results to the CSB data in Figure 1. In general, there is good agreement between CSB and CESM for all fronts across seasons. When breaking this comparison down by front type (Figure S2), a seasonal bias of fewer fronts in CESM relative to CSB does become evident in warm and occluded fronts, though those are generally less frequent. In general, cold and stationary fronts are more frequent (Figure S1) and better simulated (Figure S2). The spatial maps of the front crossing rate climatologies for CSB and CESM are shown in panels a) and c) of Figure 2. The spatial patterns show similar agreement, with the seasonal locations of the maximum front crossing rates in the western and central US generally agreeing across CESM and CSB.

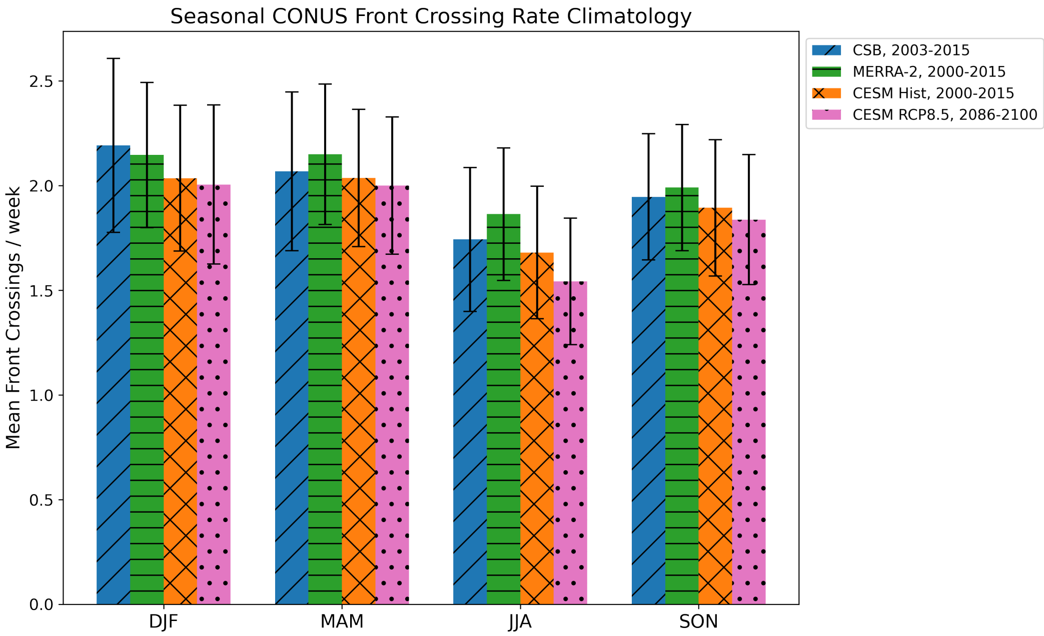

Figure 1. Seasonal CONUS averaged front crossing rate climatologies (fronts/week) for all front types. Coded Surface Bulletin (CSB) dataset (2003-2015) in blue diagonal hatching, MERRA-2 reanalysis dataset (2000-2015) in green horizontal hatching, CESM historical simulation (2000-2015) in orange cross hatching, and CESM RCP8.5 simulation (2086-2100) in pink dotted hatching. Error bars show plus or minus the standard deviation across years for each dataset.

There is a slight underestimation of overall front crossing rates in CESM, which is also reflected in the spatially averaged bar plot (Figure 1), though this is within the spatial mean standard deviation.

We further compare the CESM historical results to detected fronts in the MERRA-2 reanalysis data. Here we use MERRA-2 fields specifically chosen to better match the variables from CESM that we are using to detect fronts. Specifically, we use lowest atmospheric layer specific humidity (instead of 2-meter specific humidity), lowest atmospheric layer zonal wind (instead of 10-meter zonal wind), and lowest atmospheric layer meridional wind (instead of 10-meter meridional wind) from MERRA-2 to match the CESM variables. We also use surface temperature (instead of 2-meter air temperature) from MERRA-2 to match the CESM variable. Here we are comparing two machine learning-based climatologies (as opposed to CSB which uses hand labeled fronts). However, this is a feasible approach to further evaluate the CESM results, which would otherwise require hand labeling fronts in model output and is subject to human interpretation biases. We post-process the raw MERRA-2 fields similarly to how the CESM output is processed, and run the processed fields through DL-FRONT for 2000-2015. The resulting MERRA-2 seasonal CONUS front crossing rate climatologies are shown in Figure 1. In general, there is good agreement between MERRA-2 and CESM for all fronts across seasons. There is again a seasonal bias of fewer fronts in CESM relative to MERRA-2 for warm and occluded fronts that becomes evident when breaking down by front type (Figure S2), as well as a more pronounced positive bias in CESM stationary fronts (but within error). The corresponding spatial maps comparing MERRA-2 and CESM historical front crossing rate climatologies are shown in panels b) and c) of Figure 2. The spatial patterns are roughly similar, with the maxima located in the central U.S. There are some seasonal

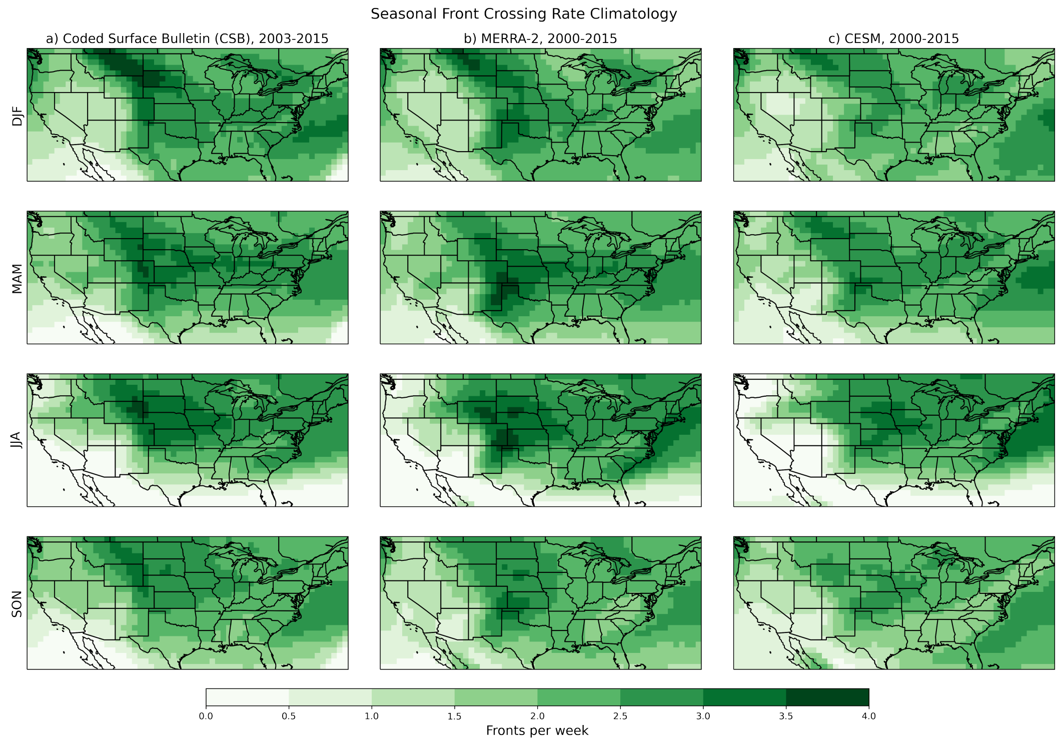

Figure 2. Seasonal front crossing rate climatologies (fronts/week) for all front types. a) Coded Surface Bulletin (CSB) dataset (2003-2015). b) MERRA-2 reanalysis dataset (2000-2015). c) CESM historical simulation (2000-2015).

differences between CESM and MERRA-2 as evident in Figure 1, though they are also within the spatial mean standard deviation.

To better evaluate different front types across datasets, we also calculate the annual mean front rates for each front type across CSB, MERRA-2, and CESM historical data (Figure S3). In general, CESM captures the magnitude of the annual mean front crossing rates for cold and stationary fronts relative to CSB and MERRA-2. The spatial pattern of more stationary fronts just east of the Rocky Mountains is consistent across datasets. However there is a positive bias of more warm and occluded fronts in CSB and MERRA-2 relative to CESM (also reflected in the spatial mean in Figure S2), in particular looking at the spatial pattern of warm fronts across the upper Midwest. The spatial pattern of cold fronts in CESM is also shifted somewhat to the northeast, relative to CSB and MERRA-2.

4 Results

4.1 Front Frequency Response to Climate Change

We next apply the CESM front detection to a future climate simulation using RCP8.5 forcing. The resulting CONUS mean seasonal front crossing rate climatologies are shown in Figure 1 for all fronts and in Figure S2 by front type. There is a slight decrease in CESM detected front rates with RCP8.5 relative to historical for all fronts across all seasons, which is most evident in JJA, but no significant changes in the spatial average. Looking across front types, the decreases are coming mostly from cold fronts with smaller changes in other fronts. However, the spatial maps for each simulation period along with the spa-

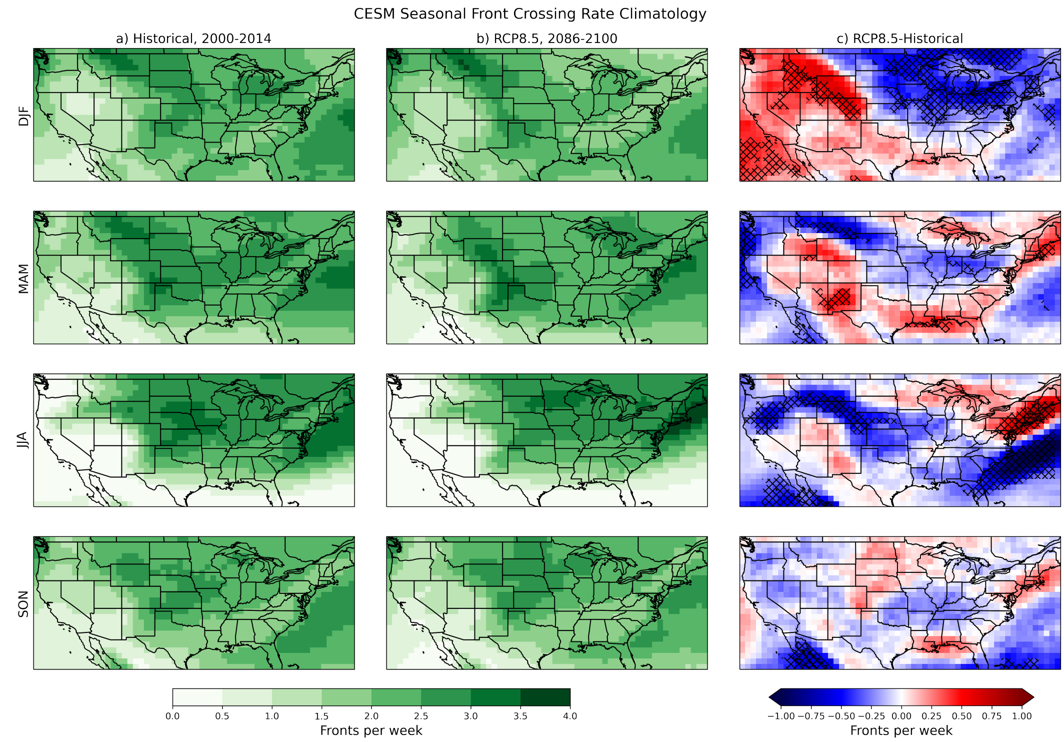

Figure 3. Seasonal front crossing rate climatologies (fronts/week) for all front types. a) CESM output for the historical simulation (2000-2014). b) CESM output for the RCP8.5 simulation (2086-2100). c) The spatial difference for each season. Hatched regions indicate changes greater than the standard deviation from the historical simulation at that gridpoint.

tial differences show notable regional changes in Figure 3. Here we calculate the CESM historical climatology from 2000 to 2014 to match the number of simulation years available from the RCP8.5 simulation (2086-2100). The difference plots indicate a westward shift in DJF and MAM front rates, and a northward shift in JJA and SON. Figures S4-7 show the spatial maps broken down by front type, where we again see that cold (Figure S4) and stationary (Figure S6) fronts are the most frequent across the CONUS, with smaller contributions from warm and occluded fronts. The difference plots indicate that changes in stationary fronts drive most of the overall seasonal shifts, though cold and warm fronts also contribute to localized changes in all seasons. In particular, there are regional decreases in cold fronts during all seasons, and significant decreases in many areas during JJA and SON. These seasonal decreases in summer and autumn indicate a potential poleward shift in cold front locations, which could have important downstream impacts.

Seasonal changes in front frequencies could be connected to large-scale circulation changes, including changes in the jet stream or extratropical cyclone tracks (e.g., Burls et al., 2019). To provide further insights into upper level atmospheric circulation that can affect extratropical cyclone development and tracks, along with associated fronts, we plot changes in seasonal upper level (300mb) zonal wind, 300mb geopotential height anomalies, and sea level pressure (SLP) for the CESM RCP8.5 simulation minus the historical simulation in Figure 4. We compare the seasonal patterns in changes in upper level height (Figure 4b) and seasonal changes in sea level pressure (Figure 4c) with changes in front crossing rates (Figure 3c). The westward shift in all front types during DJF and MAM is also evident in the shifts in upper level wind patterns, with decreases in the east-

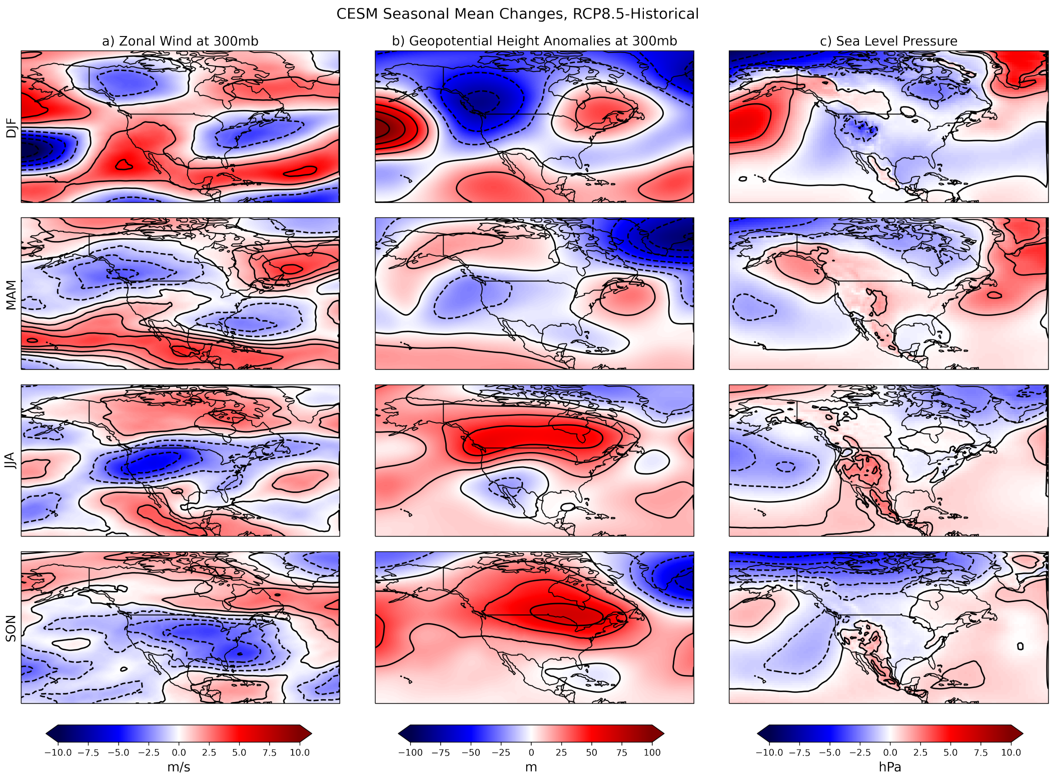

Figure 4. Seasonal mean changes in a) 300mb zonal wind speed (m/s), b) 300mb geopotential height (m, global mean difference removed from each gridpoint), and c) sea level pressure (hPa). Differences are shown with black line contours (solid for positive values and dashed for negative values) and filled contours (shading, as indicated with colorbars). All panels show the CESM RCP8.5 simulation (2068-2100) minus the CESM historical simulation (2000-2014).

ern U.S and increases in the western U.S., especially in DJF (Figure 4a). Similar increases in stationary fronts in DJF and MAM (Figure S6) are associated with an anomalous trough over the western U.S. in those seasons (Figure 4b). This anomalous trough in DJF, indicating increased storm activity, is also associated with an increase in cold fronts in the western U.S. (Figure S4). The anomalous trough weakens and shifts a bit south in MAM, and is associated with increased SLP anomalies over southern California and other parts of the western U.S. associated with changes in cold and stationary fronts there. The northward shift in all fronts in JJA and SON from Figure 3c is mirrored by broad decreases in upper level zonal wind across CONUS with increases over Canada (Figure 4a). The upper level circulation anomalies in JJA and SON indicate a broad area of positive 300mb height anomalies (Figure 4b) and anomalously high SLP in the western U.S. (Figure 4c) which would indicate more stagnant circulation and stalled fronts that would produce increases of stationary fronts (Figure S6) and decreases of cold fronts (Figure S4). By SON, the area of positive 300mb height anomalies covers almost all of North America, and is associated with a consequent increase of stationary fronts over most of the U.S. and a corresponding decrease of cold fronts.

4.2 Changes in Total Frontal Precipitation

Seasonal spatial plots of the CESM fraction of total precipitation associated with a front are shown in Figure 5 for the CONUS domain. In the eastern U.S., fronts are a

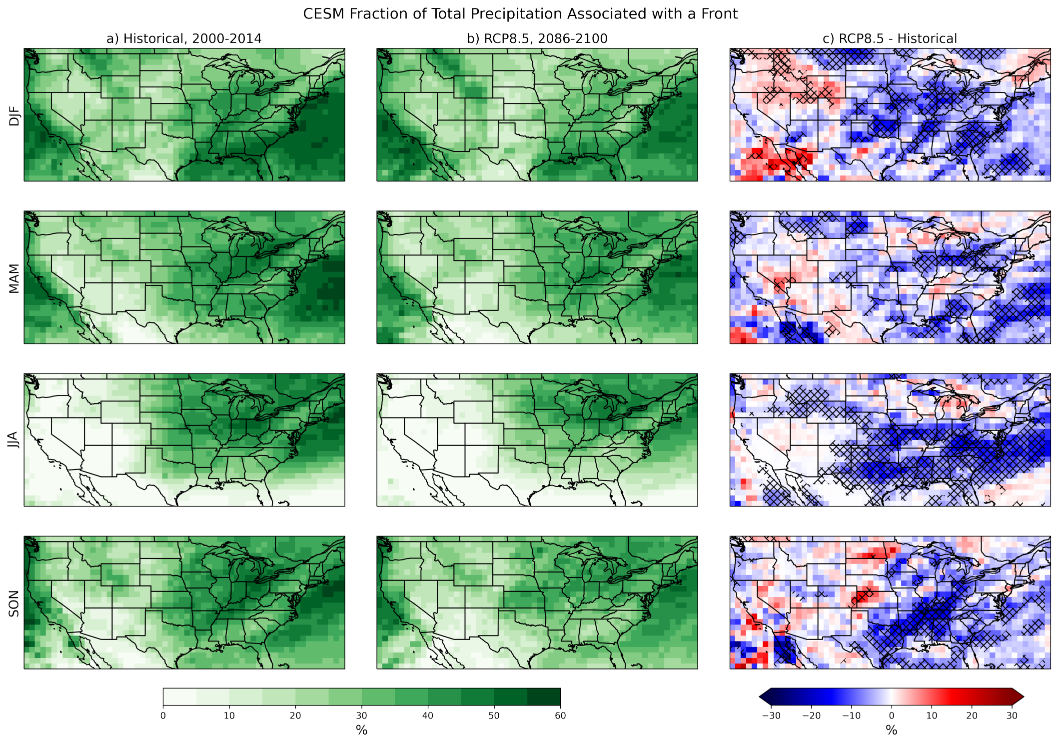

Figure 5. Fraction of total precipitation (%) associated with a front by season. a) CESM historical simulation (2000-2014). b) CESM RCP8.5 simulation (2086-2100). c) The spatial difference between CESM RCP8.5 and historical for each season. Hatched regions indicate statistical significance at the 95% confidence level using a two-tailed 1,000-member bootstrap resampling test.

large source of precipitation (40-60%) across seasons. In the western U.S., the frontal precipitation fractions are lower than in the eastern U.S., especially in JJA. The spatial patterns are similar between the historical simulation (Figure 5a) and the RCP8.5 simulation (Figure 5b), however the difference plots (Figure 5c) do show some significant seasonal changes. There are large areas of decrease (10-20%) in all seasons, particularly in the southeastern U.S. There are also a few regions of significant increases, for example the western U.S. in DJF and the central U.S. in SON.

We also calculate the fractions of total frontal precipitation separately for each front type (Figures S8-11). As noted in the discussion above, the patterns of changes in cold (Figure S4) and stationary (Figure S6) fronts are the primary drivers of the patterns of changes in all fronts (Figure 3). Similarly, cold (Figure S8) and stationary (Figure S10) fronts have higher frontal precipitation fractions relative to warm (Figure S9) and occluded (Figure S11) fronts. Cold front precipitation is concentrated in the eastern U.S. and off the East and West Coasts in all seasons, with smaller percentages in JJA. Precipitation associated with stationary fronts shows the opposite spatial pattern to cold fronts with higher percentages in JJA in the Eastern U.S., and also a specific region of high percentages in DJF over the Rocky Mountains. Warm and occluded front precipitation fractions are higher in DJF and MAM than in other seasons, and concentrated along coastlines. Looking at changes between the historical and RCP8.5 simulations, cold and stationary front precipitation fractions show more areas of significant changes than warm and occluded fronts. There are significant decreases in JJA in the southeastern U.S. for both cold and stationary front precipitation fractions. There are also significant increases in MAM in southern California for cold front precipitation fractions, and significant increases in SON in the central U.S. for stationary front precipitation fractions. Warm front precipitation fractions do show some significant increases off the coast of southern California in DJF, and the same area shows significant decreases in occluded front precipitation fractions in MAM.

The changes in total frontal precipitation due to changes in frequency and intensity (as specified by Equation 1) are shown in Figure 6 for each season. The frequency term (Figure 6a) is an important component of the total change (Figure 6c) for all seasons, while the intensity term (Figure 6b) contributes for specific regions and seasons. For example, intensity increases in the eastern U.S. in DJF cancel out decreases in frequency there and lead to total increases in frontal precipitation. However in the western U.S. in DJF the frequency term is more important to total increases in frontal precipitation there, driven by changes in cold and stationary fronts as discussed above (Figures S4 and S6). While overall there is a decrease in cold fronts over the western U.S. in MAM and an increase in SLP there (Figure 4c), the southern California coast shows the potential to have more precipitation associated with cold fronts (Figure S8). This is also reflected in the intensity increases in this region. So while cold fronts decrease in frequency in MAM in the western U.S., and increased SLP suggests fewer incoming storms, when they do arrive, they are likely more intense and could bring more moisture into the coast. Stationary fronts may be stalling out due to anomalously high SLP in MAM and JJA in the western U.S., which could help explain regions like the northern U.S. that see coincident decreases in cold fronts and increases in stationary fronts in JJA, leading to a mixed response in the total frontal precipitation changes there. Frequency decreases off the East Coast in JJA, driven by decreases in cold and stationary fronts, are particularly important for total changes in frontal precipitation. Intensity decreases in the eastern U.S. in SON are important for explaining the total decreases there, and could be related to changes in cold fronts and cold front precipitation there. We test the sensitivity of these results to removing days with total precipitation less than 1 mm, and find that while this filtering does increase the magnitude of these changes it does not significantly alter the results in terms of seasonality or spatial patterns (Figure S12).

To summarize changes in precipitation frequency and intensity terms across front types, we compute the spatial average for each term over CONUS, separately for each season and front type (Figure 7). In general, cold fronts have a negative contribution from changes in frequency which is balanced by a positive contribution from changes in intensity in all seasons except JJA. Occluded fronts also have a negative contribution from changes in frequency in all seasons except DJF, though the magnitudes of the contributions are smaller than cold fronts. Warm fronts have positive contributions from changes in intensity across all seasons, and a positive contribution from changes in frequency for DJF only (other seasons show small negative contributions in frequency). Stationary fronts have positive contributions in frequency in all seasons except JJA, and negative contributions in intensity in all seasons except DJF. While using the CONUS spatial mean helps facilitate a comparison of these changes across front types and seasons, it is worth noting that small changes in the spatial means of frequency and intensity contributions may be due to spatially varying responses with different signs getting averaged out.

4.3 Changes in Frontal Extreme Precipitation

Seasonal spatial plots of the CESM probability ratios (PR) of frontal extreme precipitation (as specified by Equation 2) are shown in Figure 8 for the CONUS domain. These plots are reminiscent of total frontal precipitation fractions in Figure 5 where in the eastern U.S. extreme precipitation is more likely to be associated with a front ($PR > 1$) across seasons. Probability ratios tend to decrease in the central and western U.S., especially in JJA, but increase again towards the West Coast in other seasons. The spatial patterns are similar across the CESM historical (Figure 8a) and RCP8.5 (Figure 8b)

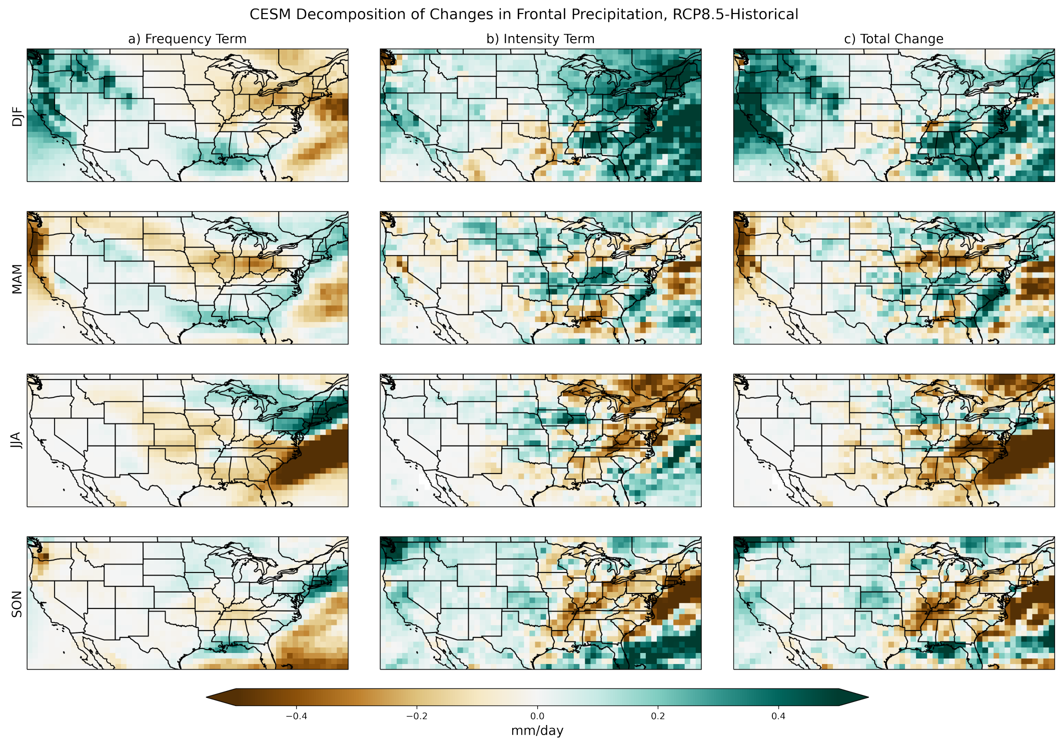

Figure 6. Decomposition of changes in frontal precipitation (mm/day) for all fronts by season. a) Frequency term: changes due to changes in front frequency. b) Intensity term: changes due to changes in frontal precipitation intensity. c) Total changes. Changes are calculated for the CESM RCP8.5 simulation (2068-2100) minus the CESM historical simulation (2000-2014).

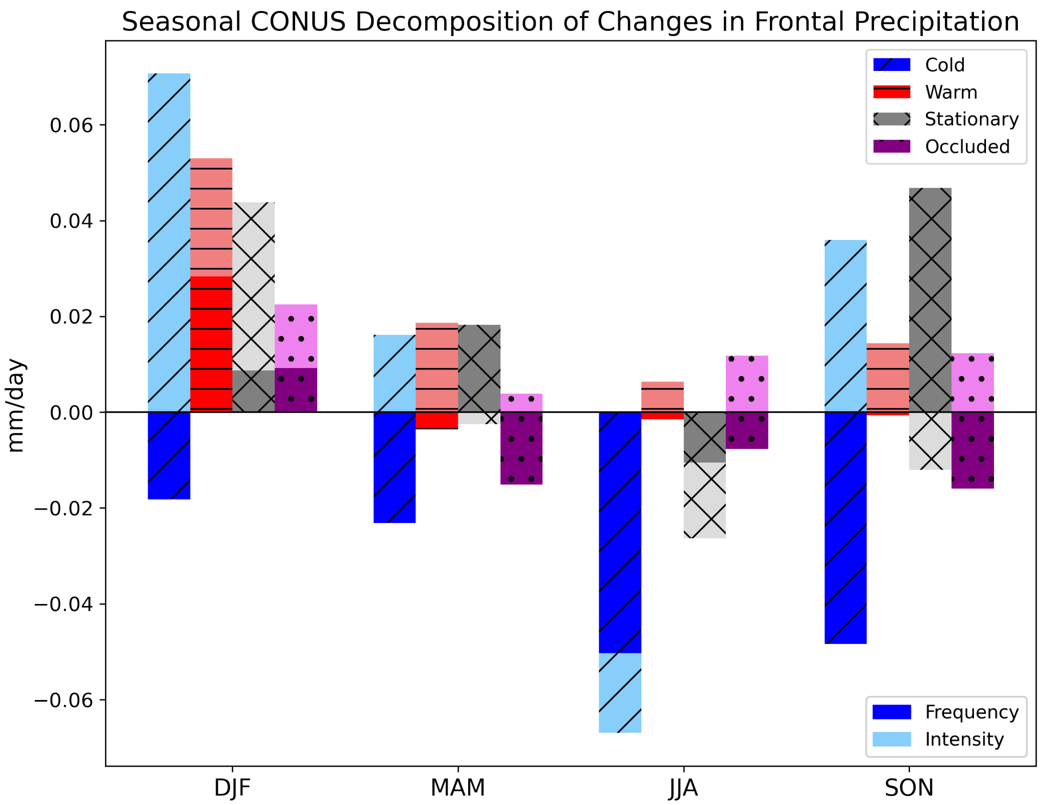

Figure 7. Seasonal CONUS averaged decomposition of changes in frontal precipitation (mm/day) for cold fronts in blue diagonal hatching, warm fronts in red horizontal hatching, stationary fronts in grey cross hatching, and occluded fronts in purple dotted hatching. The frequency term is shown in darker colors and the intensity term is shown in lighter colors. Changes are calculated for the CESM RCP8.5 simulation (2068-2100) minus the CESM historical simulation (2000-2014).

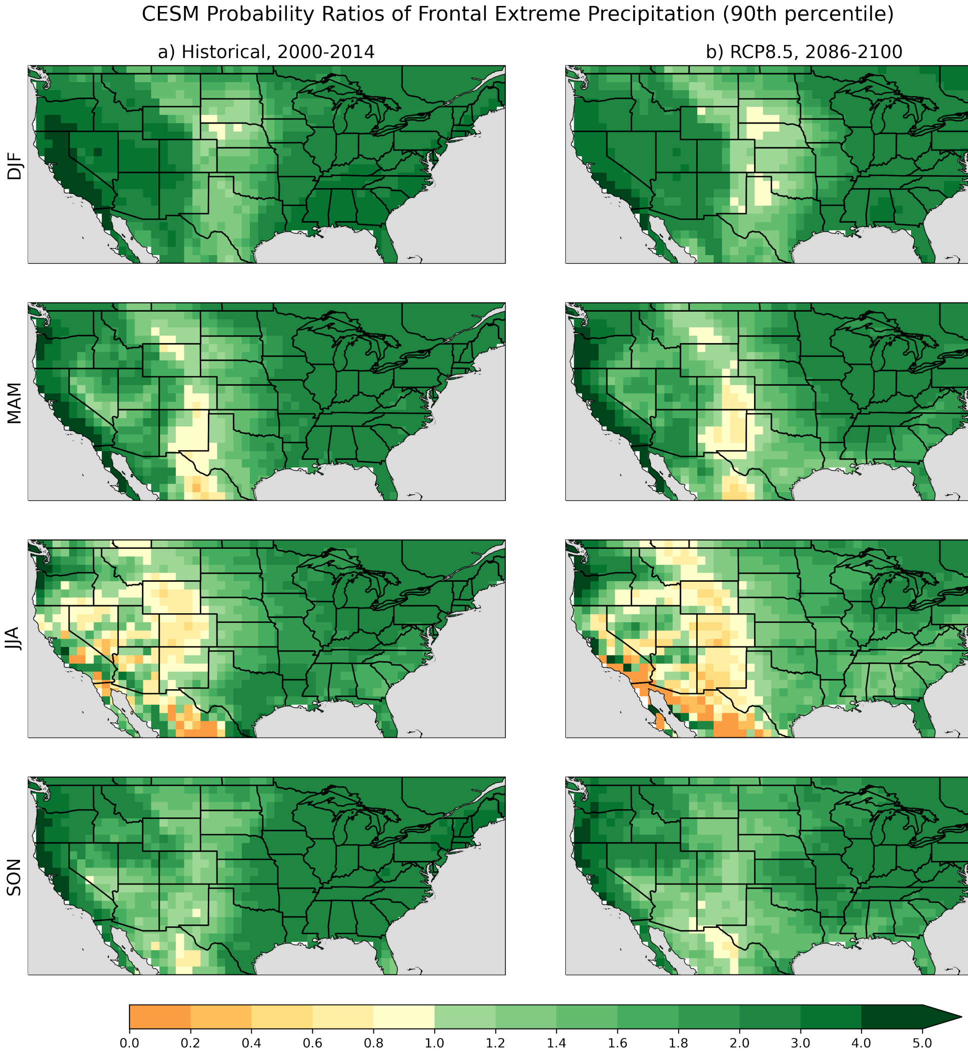

Figure 8. Probability ratios comparing the conditional probability of frontal extreme precipitation (greater than 90th percentile) over land to the climatological probability of extreme precipitation. a) CESM historical simulation (2000-2014). b) CESM RCP8.5 simulation (2086-2100).

simulations, with an expansion of the regions less likely to have frontal extreme precipitation ($PR < 1$) in all seasons under RCP8.5.

Since definitions of extreme precipitation can vary (Alexander et al., 2019; Schär et al., 2016), we test the sensitivity of the above analysis to the definition of extreme precipitation. We calculate extreme precipitation based on 95th and 99th percentiles, repeat the analysis of probability ratios, and find that the conclusions are not overly sensitive to the definition of extreme precipitation. Looking spatially, the 95th percentile results are consistent with the 90th percentile results, both in terms of areas that see lower or higher probability ratios, as well as areas that see an expansion of $PR < 1$ in the RCP8.5 simulation relative to the historical simulation (Figure S13). The 99th percentile results are also broadly consistent, though much noisier, likely due to the more extreme definition resulting in a smaller sample size (Figure S14). As with the total frontal precipitation analysis, we test the sensitivity of these results to removing days with total precipitation less than 1 mm before calculating the extreme precipitation, and find that this filtering does not significantly alter the results (not shown).

For reference, we summarize CESM changes in mean and extreme precipitation for the RCP8.5 simulation relative to the historical simulation in Figure 9. The season spatial patterns of changes in mean (Figure 9a) and extreme (Figure 9b) precipitation are similar in terms of sign, though not always in terms of relative magnitude (Allen & Ingram, 2002). Extreme precipitation is expected to increase almost everywhere over the U.S. in a warmer climate (e.g., Tebaldi et al., 2006; Sillmann, Kharin, Zwiers, et al., 2013; Akinsanola, Kooperman, Reed, et al., 2020), and this is also observed in these CESM RCP8.5 simulations. However, in certain seasons and regions, the changes in frontal-associated precipitation (Figures 5c and 6c) are often tied to changes in the fronts themselves (Figures 3c and 6a), and may not be reflected in total increases in extreme precipitation. For example, in DJF the changes in front frequency show an east-west dipole with increases in the west and decreases in the east that is not present in the changes in mean and extreme precipitation. The interplay between extreme precipitation from fronts and from other other sources is indicated by decreases in fronts and the fraction of total frontal precipitation in the upper Midwest and Northeast in DJF while there are overall significant increases of extreme precipitation in those regions. While some of this can be explained by changes in intensity (Figure 6b), processes other than fronts, such as extratropical cyclones, could also be producing the increased extreme precipitation in those regions during DJF. Changes in frontal precipitation and mean and extreme precipitation show similar overall patterns in MAM with decreases in the upper Midwest and the northwestern U.S., and increases in New England. As in DJF, areas where there are decreases in frontal precipitation and the likelihood of frontal extreme precipitation (Figure 8) and increases in total extreme precipitation (e.g., the Gulf Coast) indicate regions where processes other than fronts are producing increases in extreme precipitation. In MAM, likely candidates include mesoscale convective systems or extratropical cyclones. In JJA, there are decreases in front frequencies and frontal precipitation in the central and southeastern U.S. There is also a notable decrease in the likelihood of frontal extreme precipitation across most of the U.S. However, there is an overall increase in mean and extreme precipitation across these regions. In this season, such precipitation extremes are likely to be produced by organized convective systems, particularly in the central U.S. where the significant increases in total extreme precipitation likely have contributions from stronger convection in the North American Monsoon. Increases in mean and extreme precipitation along the Gulf Coast and southeastern U.S. in JJA could be associated with tropical cyclones. In SON, there is again an east-west dipole in changes in front frequencies and total frontal precipitation but shifted somewhat southeastward from the DJF response, with increases in the Great Plains and decreases in the southeastern U.S. There is also a decrease in the likelihood of frontal extreme precipitation in the southeastern U.S. in SON. The increases in the Great Plains would act to contribute to the total increases of mean and extreme precipitation there, while the decreases in the southeastern U.S. indicate that other processes in that region, likely associated with organized convective storms or tropical cyclones, are probably the main drivers of increased extreme precipitation there.

5 Discussion and Conclusions

In this paper we apply a deep learning algorithm (DL-FRONT) to study how seasonal changes in fronts influence total and extreme precipitation in global high resolution coupled climate model simulations with the Community Earth System Model (CESM). We show success in applying DL-FRONT to CESM output over CONUS, despite the algorithm being trained on observational and reanalysis data (Biard & Kunkel, 2019). These results provide evidence that CNNs can be applied to data products that differ from those used for training, and are thus transferable and robust for feature detection applications.

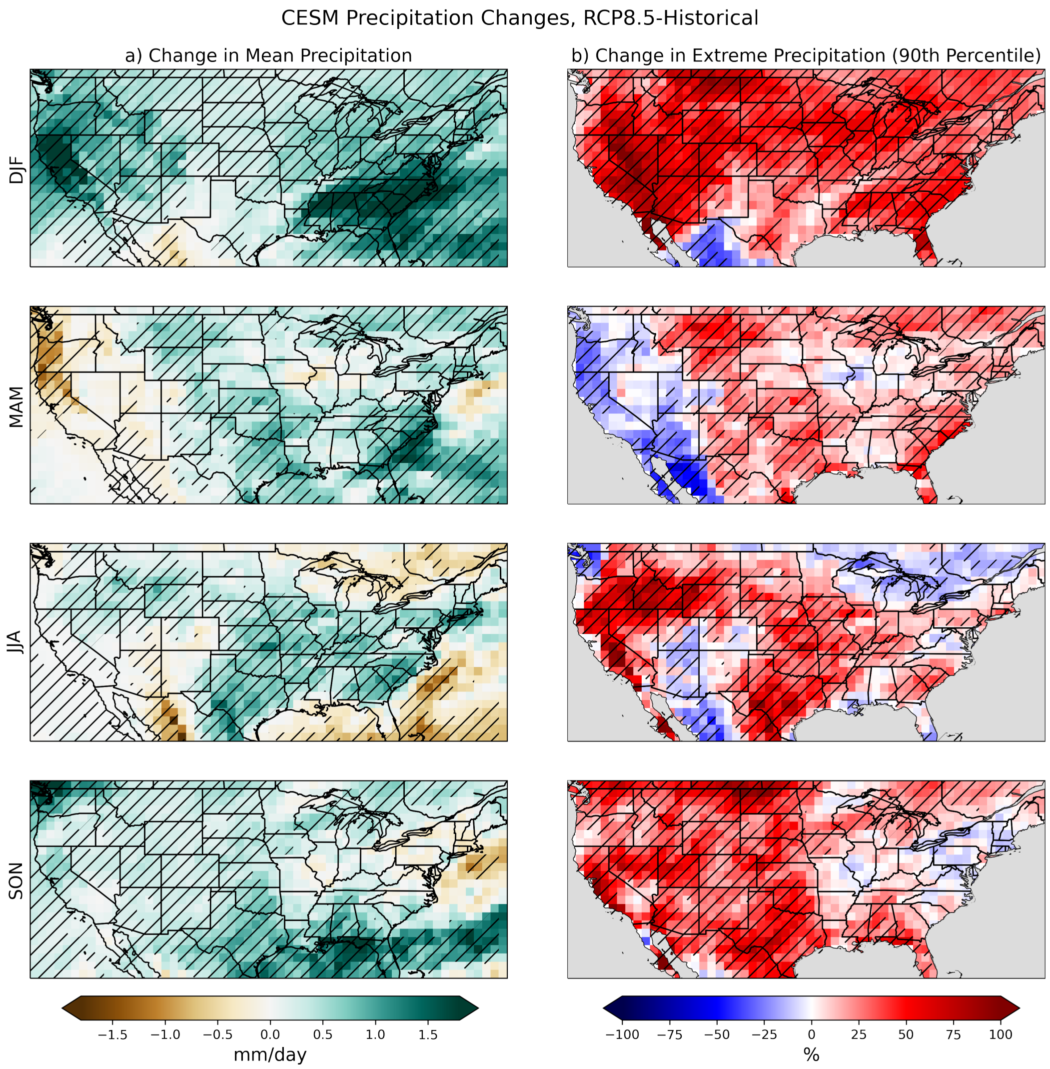

Figure 9. Seasonal mean changes in a) mean precipitation rate (mm/day) and b) total extreme precipitation (greater than 90th percentile) over land (%). Both panels show the CESM RCP8.5 simulation (2086-2100) minus the CESM historical simulation (2000-2014). Hatched regions indicate statistical significance at the 95% confidence level using a two-tailed 1,000-member bootstrap resampling test.

Furthermore, we utilize similar observational and reanalysis products to evaluate the CESM results. While it is difficult to find labeled front data, we are able to leverage an existing NWS dataset over North America, the Coded Surface Bulletin (CSB), as well as MERRA-2 reanalysis fields run through the front detector. Both the CSB and MERRA-2 seasonal front crossing rate climatologies compare well with the results from CESM (Figures 1, 2, and S2) and annual mean front crossing rates by front type exhibit similar spatial patterns across datasets (Figure S3). In the future, transfer learning through adjustments to the DL-FRONT architecture and feature importance tests to understand which variables contribute the most predictive skill could allow for applications outside the training dataset of North America. The use of other data products like high resolution ERA5 reanalysis fields could provide further insight into the evaluation of automated front detection on climate data, especially as frontal identification has been shown to vary with spatial resolution across reanalysis datasets (Soster & Parfitt, 2022) and the various factors that contribute to defining fronts (Thomas & Schultz, 2019b).

A number of previous studies have investigated fronts and precipitation in climate models. Using the ACCESS atmosphere model, Catto et al. (2013) evaluated frontal precipitation and found that front frequency and precipitation were well captured in the model, relative to ERA-Interim reanalysis. They also highlighted some regional differences between ACCESS and ERA-Interim, including fewer modeled fronts over the western U.S., which is similar to what we find comparing CSB and MERRA-2 front climatologies with CESM detected fronts (Figures 2 and S3). This result was confirmed by Catto et al. (2014) looking across CMIP5 models, where they also saw a poleward bias in the location of the Northern Hemisphere front frequency maximum. Catto et al. (2013) connected these regional differences in the Northern Hemisphere to poleward shifts in the modeled storm track and stronger pressure gradients in the model, relative to observations. This mechanism is likely also responsible for what we see in CESM relative to the MERRA-2 reanalysis, where the seasonal sea level pressure in the North Atlantic and North Pacific is higher in the model than in reanalysis, especially in JJA (Figure S15).

We find the highest front frequencies in CESM over the central U.S., or just east of the Rocky Mountains (Figure 3a, b). This result is consistent with annual mean front frequencies from Berry, Jakob, and Reeder (2011) where they looked across four different reanalysis products, and linked areas with high front frequencies to persistent baroclinic zones produced by changes in terrain. Schemm et al. (2015) also saw a peak in DJF front frequency east of the Rocky Mountains in ERA-Interim reanalysis, though it was more pronounced using a wind-based detection method relative to a temperature-based method, demonstrating an important sensitivity to variables used in front detection. Lagerquist et al. (2020) calculated front frequencies using a machine learning method applied to ERA5 reanalysis, and also showed that North American winter cold fronts have the highest frequency downwind of the Rockies and are related to cyclonic activity. They found a local maximum of winter warm fronts over the Great Lakes region, and summer warm fronts over the northern Plains. Thomas and Schultz (2019a) found a relative minimum in summertime fronts over southern North America, looking at ERA-Interim reanalysis. We see similar features in Figures S4-5 looking at CESM seasonal cold and warm front rate climatologies.

Our results comparing CESM front frequencies across historical and future climate change simulations show seasonally and spatially varying patterns and responses to climate change, with some decreases evident in all seasons (Figure 3c). This is similar to what other studies have found regarding historical trends in North American fronts. For example, Berry, Jakob, and Reeder (2011) found a 10-20% decrease in front frequency in the North Atlantic storm track from 1989-2009 using four independent reanalysis products. They related these trends to a poleward shift of the Northern Hemisphere storm track. Rudeva and Simmonds (2015) also found a northward shift of frontal activity in the Northern Hemisphere, looking at ERA-Interim reanalysis from 1979-2013, and linked these changes to modes of variability such as the North Atlantic Oscillation (NAO) and El Niño-Southern Oscillation (ENSO). Significant positive correlations between fronts and the NAO were found in Northern Hemisphere winter (DJF) over North America, with decreases in DJF front frequency across the eastern U.S. associated with ENSO (Rudeva & Simmonds, 2015). We also find significant decreases in DJF front frequency across most of the central and eastern U.S. with climate change (Figure 3c). Lagerquist et al. (2020) analyzed historical trends in front frequencies from 1979-2018 and found consistent results with previous analyses, including poleward shifts in winter and spring frontal activity. They also found a decrease in summer and increase in winter cold front lengths, possibly driven by a lack of cold air reaching the southeastern U.S. and more cold air reaching the western U.S., respectively, as well as a strong connection to ENSO phase and intensity (Lagerquist et al., 2020). These regional changes in front length are consistent with the seasonal changes in all front crossing rates in Figure 3c and more specifically cold and stationary front crossing rates in Figures S4 and S6, with decreases in JJA over the southeastern U.S. and increases in DJF over the western U.S. Connecting changes in fronts and other synoptic features to changes in modes of variability will be the focus of future work.

While there are consistencies between our results and previous studies looking at historical trends in fronts, recent historical trends are not the same as the projected climate change signal from an RCP8.5 simulation at the end of the century. Catto et al. (2014) analyzed changes in front frequencies under RCP8.5 in CMIP5 simulations and found annual mean decreases over most of CONUS with small increases in the northeastern U.S., largely consistent with what we see across seasons. Barnes and Screen (2015) looked at the impact of future warming on the midlatitude jet stream, and found a poleward shift of the North Atlantic jet in all seasons except winter, looking across 21 CMIP5 models under RCP8.5 at the end of the century. Osman et al. (2021) used paleoclimate data to assess the role of natural variability in projections of North Atlantic jet stream position and intensity, and found further evidence of a northward migration of the jet during the 21st century. These results are consistent with the northward shift in front frequencies (Figure 3c), decreases in upper level zonal wind (Figure 4a), and positive 300mb height anomalies across the northern CONUS (Figure 4b) that we see in JJA and SON for CESM under RCP8.5. If the jet stream is trending north due to a warmer climate, extratropical cyclones may also stay farther north. This signal could result in both decreases in cold fronts (Figure S4) and increases in stationary fronts (Figure S6) over more southern latitudes, as cold air masses could stall due to being farther away from the extratropical cyclone support at those more southern latitudes. The responses in winter and spring could be related to the seasonality of the North Pacific storm track and its influence over the western U.S. (Breeden et al., 2021; Newman & Sardeshmukh, 1998; Hoskins & Hodges, 2019), which would help explain the westward shift in maximum front frequencies (Figure 3c), particularly in cold and stationary fronts, and shifts in corresponding circulation patterns (Figure 4) we see in DJF and MAM. With regard to changes in specific front types with climate change, we note that Biard and Kunkel (2019) showed DL-FRONT had some difficulty distinguishing between cold and stationary fronts, adding some uncertainty in the projections of each front type. Assessing the sensitivity of a deep learning model like DL-FRONT to climate change conditions, while out of scope for this current study, is an important consideration for future work (Molina et al., 2021).

We find that modeled frontal precipitation has a broader spatial pattern over CONUS in the winter than in the summer (Figure 5a, b). This result is consistent with studies relating total precipitation to fronts, where a maximum is observed in Northern Hemisphere winter that reduces to a minimum in summer (Catto et al., 2012; Hénin et al., 2019). This seasonality is related to shifts in the midlatitude storm track, as discussed above. Our results also show that modeled frontal precipitation is more common in the central and eastern U.S. in all seasons, and this is especially driven by cold (Figure S8) and stationary (Figure S10) frontal precipitation. Catto and Pfahl (2013) also found that cold fronts were responsible for a larger proportion of precipitation events, relative to warm and quasi-stationary fronts. Hénin et al. (2019) found that warm fronts were important for precipitation over the Great Lakes region, consistent with the local maximum in warm front precipitation we see in this region in Figure S9. Using probability ratios, we find that frontal extreme precipitation is more likely over the eastern U.S. in all seasons, and also more likely over the West Coast in all seasons except JJA (Figure 8). Catto and Pfahl (2013) found a similar spatial pattern looking at ERA-Interim extreme precipitation, where greater than 70% of extreme precipitation events in the eastern U.S. were associated with fronts (noting that they defined extreme precipitation as greater than the 99th percentile). They also found higher percentages in DJF compared to JJA, consistent with the seasonality of fronts and frontal extreme precipitation. Using weather station data, Kunkel et al. (2012) found that fronts accounted for 54% of U.S. extreme precipitation events in the last 100 years, with locally higher percentages across the central U.S., comparable to what we see in our analysis.

Our results show that the fraction of total precipitation associated with fronts over CONUS mostly decreases with climate change, though there are some localized increases in certain seasons (Figure 5c). These decreases are driven mostly by cold (Figure S8) and stationary (Figure S10) fronts, similar to what Hénin et al. (2019) found in the North Atlantic region where cold fronts were more important than warm fronts in explaining trends in frontal precipitation. Despite the decreases in frontal precipitation fractions, we also find general increases in mean and extreme precipitation over most of the U.S. under the RCP8.5 simulation (Figure 9). When analyzing the decomposition of frontal precipitation changes, we find total increases in DJF driven mostly by changes in intensity, total decreases in JJA driven mostly by changes in frequency, and mixed responses in other seasons (Figures 6, 7). Utsumi et al. (2016) saw simultaneous decreases in the annual mean frequency of front precipitation and increases in front precipitation intensity across all of CONUS in CMIP5 simulations, though they also included extratropical cyclones in their analysis. Burls et al. (2019) looked at Southern Hemisphere winter fronts and rain days in ERA-Interim from 1979-2017, and found a decrease in rain days associated with fronts despite no significant changes in front days. They related these changes to a poleward shift in the subtropical high as well as an increase in intensity of post-frontal high pressure. Pepler et al. (2021) investigated changes in Australian rainfall over the past several decades and also found that the amount of frontal precipitation has decreased while there is little change in number of fronts. This result is driven by a simultaneous decrease in rainfall-producing fronts and increase in dry fronts. While we see significant changes in both front frequencies and precipitation associated with fronts, it is possible that these historical trends in the Southern Hemisphere related to midlatitude circulation, such as the Hadley Cell expansion (Burls et al., 2019; Amaya et al., 2018), could be influencing the changes we see in modeled North American frontal total and extreme precipitation. Furthermore, we see decreases in the likelihood of frontal extreme precipitation across seasons and especially in JJA (Figure 8). While extreme precipitation is increasing in the model with climate change, frontal precipitation is largely decreasing and frontal extreme precipitation is becoming less likely. These changes are related to the seasonal shifts in front frequency, and in particular changes in cold and stationary fronts. This result also points to the importance of other sources of extreme precipitation over the U.S. (Huang et al., 2018), and the difficulty of disentangling total and extreme precipitation from converging sources (Kunkel et al., 2012; Kunkel & Champion, 2019; Blázquez & Solman, 2019). It is also important to note that model projections of frontal precipitation may be influenced by compensating errors in frequency and intensity, as shown in Catto, Jakob, and Nicholls (2015) evaluating wintertime frontal precipitation in CMIP5 models and Leung et al. (2022) with CMIP6 models. However Leung et al. (2022) noted that CMIP6 models on average appear to have smaller errors, indicating some potential improvement in model biases.

This study focuses on fronts only, though fronts are often associated with other synoptic-scale features such as extratropical cyclones (ETCs) (Catto & Pfahl, 2013) and warm conveyor belts (WCBs) (Catto, Madonna, et al., 2015). Schemm et al. (2018) characterized two types of frontal-associated ETCs based on whether there is an associated front 1) at cyclogenesis, or 2) acquired during its lifecycle. ETCs initially associated with a front are most common in the Northern Hemisphere storm track regions, including the eastern U.S., whereas late-front cyclones have a higher occurrence downwind of the Rocky Mountains, though some of these regional details depend on the method used to detect fronts (Schemm et al., 2018). Catto and Pfahl (2013) found that many extreme precipitation events located in storm track regions are associated with both an ETC and a front, and even the "front-only" events can be linked to a cyclone at some point along their length. Catto, Madonna, et al. (2015) combined front identification with WCBs and found that the majority of midlatitude extreme precipitation events are linked to cold or warm fronts, and most of those fronts have associated WCBs. Dowdy and Catto (2017) investigated a "triple storm type" made up of a cyclone, front, and thunderstorm, and found that this event type is associated with the highest risk of extreme precipitation, related to environmental conditions like convective available potential energy. In the Northern midlatitudes in particular, extreme precipitation is caused most often by some combination of cyclones, fronts, and thunderstorms despite a "front-only" event type being the most frequent at these latitudes (Dowdy & Catto, 2017). It is likely that other event types, especially ETCs and mesoscale convective systems, are contributing to the extreme precipitation we see in the model as well as how mean and extreme precipitation are changing with climate change (Figure 9). The use of machine learning and climate models to capture multiple synoptic-scale features in the context of extreme precipitation will be the focus of future study.

The ability of the climate model to simulate total and extreme precipitation in both present day and future climates is important to consider. Previous studies using CMIP5 and CMIP6 models found that the multi-model mean better captured extreme precipitation than individual models, relative to present day observational datasets, likely due to compensating errors (Sillmann, Kharin, Zhang, et al., 2013; Akinsanola, Kooperman, Pendergrass, et al., 2020; Srivastava et al., 2020). Looking across CMIP6, Akinsanola, Kooperman, Pendergrass, et al. (2020) and Srivastava et al. (2020) found that several individual models, including CESM2, exhibited a summertime dry bias over the eastern U.S. and a wintertime wet bias over the western U.S., which they linked to biases in orographic and convective processes. Leung et al. (2022) found that CMIP6 models were able to well represent the spatial patterns of daily precipitation and duration of dry spells, implying these models would also be able to capture precipitation extremes. Continued model improvements in resolution (Wehner et al., 2014; Bador et al., 2020), calibration (Yang et al., 2012) and process representation such as convective precipitation (Harding et al., 2013) and atmospheric circulation (Shepherd, 2014; Priestley & Catto, 2022) may help address these biases and aid in the assessment of extreme precipitation associated with fronts.

When examining projected changes in extremes across CMIP5 models, Sillmann, Kharin, Zwiers, et al. (2013) found that extreme precipitation generally increases in most regions including North America. Looking specifically at projected changes in U.S. extreme precipitation across CMIP6 models, Akinsanola, Kooperman, Reed, et al. (2020) found consistent increases in heavy and very heavy winter precipitation days, with less agreement in summer. Robust increases in winter aligns with what we see in the changes in CESM extreme precipitation (defined as greater than 90th percentile) over the U.S. (Figure 9b). While we see significant increases across the U.S. in all seasons, some seasonal variations begin to emerge in MAM and JJA, highlighting the importance of analyzing seasonal (rather than annual mean) responses. Furthermore, the changes in extreme precipitation in a model can be sensitive to the definition of extreme precipitation (Barlow et al., 2019; Pendergrass, 2018; Zhang et al., 2011). Here we define extreme precipitation as any precipitation greater than the 90th percentile, and investigate changes over space and time. The seasonal spatial patterns of the likelihood of frontal extreme precipitation are generally consistent when using more extreme metrics to define extreme precipitation (Figures S13-S14), though some regions (e.g., the West Coast) show an increase in likelihood when using a more extreme threshold, consistent with previous work (Utsumi et al., 2016). Future work could consider how adding a temporal or spatial buffer to the definition of extreme precipitation or fronts (rather than matching exact gridpoints in space and time) impacts the resulting frontal precipitation (Catto & Pfahl, 2013).

In summary, our results demonstrate how machine learning-enabled automated detection of synoptic weather features, specifically fronts, can enable greater understanding of seasonal and regional precipitation sources and mechanisms. Leveraging the power of automated front detection, we discuss the mechanisms related to the seasonality of different front types and projected changes due to climate change. We find seasonal differences in total frontal precipitation changes across CONUS driven by the relative importance of changes in frontal precipitation frequency and intensity. By investigating modeled changes in total and extreme frontal precipitation, we advance the understanding of extreme precipitation events, their intersection with frontal systems of different types, and how those associations are changing with climate change.

6 Open Research

The Coded Surface Bulletin (CSB) dataset is available here: `https://zenodo.org/record/2642801` (National Weather Service, 2019) in ASCII format, and here: `https://doi.org/10.5281/zenodo.2651361` (Biard, 2019) in netCDF format. The MERRA-2 datasets used in this study can be downloaded via the NASA Goddard Earth Sciences (GES) Data and Information Services Center (DISC) here: `https://disc.gsfc.nasa.gov/`. All CESM simulation output used in the analysis is available through the NCAR Geoscience Data Exchange (GDEX) and published under the following DOI: `https://doi.org/10.5065/q6t7-ta06` (Dagon et al., 2022). Software being actively developed for this study is available through GitHub: `https://github.com/katiedagon/ML-extremes`.

Acknowledgments

This material is based upon work supported by the U.S. Department of Energy (DOE), Office of Science, Office of Biological & Environmental Research (BER), Regional and Global Model Analysis (RGMA) component of the Earth and Environmental System Modeling Program under Award Number DE-SC0022070 and National Science Foundation (NSF) IA 1947282. This work was also supported by the National Center for Atmospheric Research (NCAR), which is a major facility sponsored by the NSF under Cooperative Agreement No. 1852977 and by NOAA through the Cooperative Institute for Satellite Earth System Studies under Cooperative Agreement NA19NES4320002. The CESM project is supported primarily by the National Science Foundation (NSF). Computing and data storage resources were provided by the Computational and Information Systems Laboratory (CISL) at NCAR. An award of computer time was provided by the Innovative and Novel Computational Impact on Theory and Experiment (INCITE) program. This research used resources of the Argonne Leadership Computing Facility, which is a DOE Office of Science User Facility supported under Contract DE-AC02-06CH11357. This research is also part of the Blue Waters sustained-petascale computing project, which is supported by the NSF (Awards OCI-0725070 and ACI-1238993) and the state of Illinois. Blue Waters is a joint effort of the University of Illinois at Urbana-Champaign and its National Center for Supercomputing Applications. This work is also part of the "High Resolution Earth System Modeling Using Blue Waters Capabilities" PRAC allocation support by the National Science Foundation (Award ACI-1516624). This research used resources of the National Energy Research Scientific Computing Center (NERSC), a U.S. Department of Energy Office of Science User Facility located at Lawrence Berkeley National Laboratory, operated under Contract No. DE-AC02-05CH11231. We thank Melissa Breeden for useful conversations that informed this work, and Nan Rosenbloom, Gary Strand, and Susan Bates for assistance with managing CESM data.

References

Akinsanola, A. A., Kooperman, G. J., Pendergrass, A. G., Hannah, W. M., & Reed, K. A. (2020, aug). Seasonal representation of extreme precipitation indices over the United States in CMIP6 present-day simulations. *Environmental Research Letters*, *15*(9), 094003. Retrieved from `https://doi.org/10.1088/1748-9326/ab92c1` doi: 10.1088/1748-9326/ab92c1

Akinsanola, A. A., Kooperman, G. J., Reed, K. A., Pendergrass, A. G., & Hannah, W. M. (2020, oct). Projected changes in seasonal precipitation extremes over the United States in CMIP6 simulations. *Environmental Research Letters*, *15*(10), 104078. Retrieved from `https://doi.org/10.1088/1748-9326/abb397` doi: 10.1088/1748-9326/abb397

Alexander, L. V., Fowler, H. J., Bador, M., Behrangi, A., Donat, M. G., Dunn, R., ... Venugopal, V. (2019, dec). On the use of indices to study extreme precipitation on sub-daily and daily timescales. *Environmental Research Letters*, *14*(12), 125008. Retrieved from `https://doi.org/10.1088/1748-9326/ab51b6` doi: 10.1088/1748-9326/ab51b6

Allen, M. R., & Ingram, W. J. (2002). Constraints on future changes in climate and the hydrologic cycle. *Nature*, *419*(6903), 228–232. Retrieved from `https://doi.org/10.1038/nature01092` doi: 10.1038/nature01092

Amaya, D. J., Siler, N., Xie, S.-P., & Miller, A. J. (2018). The interplay of internal and forced modes of Hadley Cell expansion: lessons from the global warming hiatus. *Climate Dynamics*, *51*(1), 305–319. Retrieved from `https://doi.org/10.1007/s00382-017-3921-5` doi: 10.1007/s00382-017-3921-5

American Meteorological Society Glossary of Meteorology: Front. (n.d.). `https://glossary.ametsoc.org/wiki/Front`. (Last Access: 26 January 2022)

Bador, M., Boé, J., Terray, L., Alexander, L. V., Baker, A., Bellucci, A., ... Vanniere, B. (2020). Impact of Higher Spatial Atmospheric Resolution on Precipitation Extremes Over Land in Global Climate Models. *Journal of Geophysical Research: Atmospheres*, *125*(13), e2019JD032184. Retrieved from `https://agupubs.onlinelibrary.wiley.com/doi/abs/10.1029/2019JD032184` doi: https://doi.org/10.1029/2019JD032184

Barlow, M., Gutowski, W. J., Gyakum, J. R., Katz, R. W., Lim, Y.-K., Schumacher, R. S., ... Min, S.-K. (2019). North American extreme precipitation events and related large-scale meteorological patterns: a review of statistical methods, dynamics, modeling, and trends. *Climate Dynamics*, *53*(11), 6835–6875. Retrieved from `https://doi.org/10.1007/s00382-019-04958-z` doi: 10.1007/s00382-019-04958-z

Barnes, E. A., & Screen, J. A. (2015). The impact of Arctic warming on the midlatitude jet-stream: Can it? Has it? Will it? *WIREs Climate Change*, *6*(3), 277-286. Retrieved from `https://wires.onlinelibrary.wiley.com/doi/abs/10.1002/wcc.337` doi: https://doi.org/10.1002/wcc.337

Berry, G., Jakob, C., & Reeder, M. (2011). Recent global trends in atmospheric fronts. *Geophysical Research Letters*, *38*(21). Retrieved from `https://agupubs.onlinelibrary.wiley.com/doi/abs/10.1029/2011GL049481` doi: https://doi.org/10.1029/2011GL049481

Berry, G., Reeder, M. J., & Jakob, C. (2011). A global climatology of atmospheric fronts. *Geophysical Research Letters*, *38*(4). Retrieved from `https://agupubs.onlinelibrary.wiley.com/doi/abs/10.1029/2010GL046451` doi: https://doi.org/10.1029/2010GL046451

Biard, J. C. (2019, April). *National Weather Service Coded Surface Bulletins, 2003- (netCDF format)* [dataset]. Zenodo. Retrieved from `https://doi.org/10.5281/zenodo.2651361` doi: 10.5281/zenodo.2651361

Biard, J. C., & Kunkel, K. E. (2019). Automated detection of weather fronts using a deep learning neural network. *Advances in Statistical Climatology, Meteorology and Oceanography*, *5*(2), 147–160. Retrieved from `https://ascmo.copernicus.org/articles/5/147/2019/` doi: 10.5194/ascmo-5-147-2019

Bitsa, E., Flocas, H. A., Kouroutzoglou, J., Galanis, G., Hatzaki, M., Latsas, G., ... Simmonds, I. (2021). A Mediterranean cold front identification scheme combining wind and thermal criteria. *International Journal of Climatology*, *41*(15), 6497-6510. Retrieved from `https://rmets.onlinelibrary.wiley.com/doi/abs/10.1002/joc.7208` doi: https://doi.org/10.1002/joc.7208

Blázquez, J., & Solman, S. A. (2019). Relationship between projected changes in precipitation and fronts in the austral winter of the Southern Hemisphere from a suite of CMIP5 models. *Climate Dynamics*, *52*(9), 5849–5860. Retrieved from `https://doi.org/10.1007/s00382-018-4482-y` doi: 10.1007/s00382-018-4482-y

Breeden, M. L., Butler, A. H., Albers, J. R., Sprenger, M., & Langford, A. O. (2021). The spring transition of the North Pacific jet and its relation to deep stratosphere-to-troposphere mass transport over western North America. *Atmospheric Chemistry and Physics*, *21*(4), 2781–2794. Retrieved from `https://acp.copernicus.org/articles/21/2781/2021/` doi: 10.5194/acp-21-2781-2021

Burls, N. J., Blamey, R. C., Cash, B. A., Swenson, E. T., Fahad, A. a., Bopape, M.-J. M., ... Reason, C. J. C. (2019). The Cape Town "Day Zero"drought and Hadley cell expansion. *npj Climate and Atmospheric Science*, *2*(1), 27. Retrieved from `https://doi.org/10.1038/s41612-019-0084-6` doi: 10.1038/s41612-019-0084-6

Catto, J. L., Jakob, C., Berry, G., & Nicholls, N. (2012). Relating global precipitation to atmospheric fronts. *Geophysical Research Letters*, *39*(10). Retrieved from `https://agupubs.onlinelibrary.wiley.com/doi/abs/10.1029/2012GL051736` doi: https://doi.org/10.1029/2012GL051736

Catto, J. L., Jakob, C., & Nicholls, N. (2013). A global evaluation of fronts and precipitation in the ACCESS model. *Australian Meteorological and Oceanographic Journal*, *63*, 191–203.

Catto, J. L., Jakob, C., & Nicholls, N. (2015). Can the CMIP5 models represent winter frontal precipitation? *Geophysical Research Letters*, *42*(20), 8596-8604. Retrieved from `https://agupubs.onlinelibrary.wiley.com/doi/abs/10.1002/2015GL066015` doi: https://doi.org/10.1002/2015GL066015

Catto, J. L., Madonna, E., Joos, H., Rudeva, I., & Simmonds, I. (2015). Global Relationship between Fronts and Warm Conveyor Belts and the Impact on Extreme Precipitation. *Journal of Climate*, *28*(21), 8411 - 8429. Retrieved from `https://journals.ametsoc.org/view/journals/clim/28/21/jcli-d-15-0171.1.xml` doi: 10.1175/JCLI-D-15-0171.1

Catto, J. L., Nicholls, N., Jakob, C., & Shelton, K. L. (2014). Atmospheric fronts in current and future climates. *Geophysical Research Letters*, *41*(21), 7642-7650. Retrieved from `https://agupubs.onlinelibrary.wiley.com/doi/abs/10.1002/2014GL061943` doi: https://doi.org/10.1002/2014GL061943

Catto, J. L., & Pfahl, S. (2013). The importance of fronts for extreme precipitation. *Journal of Geophysical Research: Atmospheres*, *118*(19), 10,791-10,801. Retrieved from `https://agupubs.onlinelibrary.wiley.com/doi/abs/10.1002/jgrd.50852` doi: https://doi.org/10.1002/jgrd.50852

Dagon, K., Truesdale, J., Rosenbloom, N., & Bates, S. (2022, April). *Machine learning-based detection of weather fronts and associated extreme precipitation in CESM1.3* [dataset]. UCAR/NCAR - GDEX. Retrieved from https://doi.org/10.5065/q6t7-ta06 doi: 10.5065/q6t7-ta06

Danabasoglu, G., Bates, S. C., Briegleb, B. P., Jayne, S. R., Jochum, M., Large, W. G., ... Yeager, S. G. (2012). The CCSM4 Ocean Component. *Journal of Climate*, *25*(5), 1361 - 1389. Retrieved from https://journals.ametsoc.org/view/journals/clim/25/5/jcli-d-11-00091.1.xml doi: 10.1175/JCLI-D-11-00091.1

Dennis, J. M., Edwards, J., Evans, K. J., Guba, O., Lauritzen, P. H., Mirin, A. A., ... Worley, P. H. (2012). CAM-SE: A scalable spectral element dynamical core for the Community Atmosphere Model. *The International Journal of High Performance Computing Applications*, *26*(1), 74-89. Retrieved from https://doi.org/10.1177/1094342011428142 doi: 10.1177/1094342011428142

Dowdy, A. J., & Catto, J. L. (2017). Extreme weather caused by concurrent cyclone, front and thunderstorm occurrences. *Scientific Reports*, *7*(1), 40359. Retrieved from https://doi.org/10.1038/srep40359 doi: 10.1038/srep40359

Fischer, E. M., & Knutti, R. (2015). Anthropogenic contribution to global occurrence of heavy-precipitation and high-temperature extremes. *Nature Climate Change*, *5*(6), 560–564. Retrieved from https://doi.org/10.1038/nclimate2617 doi: 10.1038/nclimate2617

Gelaro, R., McCarty, W., Suárez, M. J., Todling, R., Molod, A., Takacs, L., ... Zhao, B. (2017). The Modern-Era Retrospective Analysis for Research and Applications, Version 2 (MERRA-2). *Journal of Climate*, *30*(14), 5419 - 5454. Retrieved from https://journals.ametsoc.org/view/journals/clim/30/14/jcli-d-16-0758.1.xml doi: 10.1175/JCLI-D-16-0758.1

Harding, K. J., Snyder, P. K., & Liess, S. (2013). Use of dynamical downscaling to improve the simulation of Central U.S. warm season precipitation in CMIP5 models. *Journal of Geophysical Research: Atmospheres*, *118*(22), 12,522-12,536. Retrieved from https://agupubs.onlinelibrary.wiley.com/doi/abs/10.1002/2013JD019994 doi: https://doi.org/10.1002/2013JD019994

Hénin, R., Ramos, A. M., Schemm, S., Gouveia, C. M., & Liberato, M. L. R. (2019). Assigning precipitation to mid-latitudes fronts on sub-daily scales in the North Atlantic and European sector: Climatology and trends. *International Journal of Climatology*, *39*(1), 317-330. Retrieved from https://rmets.onlinelibrary.wiley.com/doi/abs/10.1002/joc.5808 doi: https://doi.org/10.1002/joc.5808

Hewson, T. D. (1998). Objective fronts. *Meteorological Applications*, *5*(1), 37-65. Retrieved from https://rmets.onlinelibrary.wiley.com/doi/abs/10.1017/S1350482798000553 doi: https://doi.org/10.1017/S1350482798000553

Hope, P., Keay, K., Pook, M., Catto, J., Simmonds, I., Mills, G., ... Berry, G. (2014). A Comparison of Automated Methods of Front Recognition for Climate Studies: A Case Study in Southwest Western Australia. *Monthly Weather Review*, *142*(1), 343 - 363. Retrieved from https://journals.ametsoc.org/view/journals/mwre/142/1/mwr-d-12-00252.1.xml doi: 10.1175/MWR-D-12-00252.1

Hoskins, B. J., & Hodges, K. I. (2019). The Annual Cycle of Northern Hemisphere Storm Tracks. Part II: Regional Detail. *Journal of Climate*, *32*(6), 1761 - 1775. Retrieved from https://journals.ametsoc.org/view/journals/clim/32/6/jcli-d-17-0871.1.xml doi: 10.1175/JCLI-D-17-0871.1

Huang, H., Winter, J. M., & Osterberg, E. C. (2018). Mechanisms of Abrupt Extreme Precipitation Change Over the Northeastern United States. *Journal of Geophysical Research: Atmospheres*, *123*(14), 7179-7192. Retrieved from https://agupubs.onlinelibrary.wiley.com/doi/abs/10.1029/2017JD028136 doi: https://doi.org/10.1029/2017JD028136

Hunke, E. C., & Lipscomb, W. H. (2008). *CICE: the Los Alamos Sea Ice Model Documentation and Software User's Manual, Version 4* (Tech. Rep. No. LA-CC-06-012). Los Alamos National Laboratory.

Krizhevsky, A., Sutskever, I., & Hinton, G. E. (2012). ImageNet Classification with Deep Convolutional Neural Networks. In F. Pereira, C. Burges, L. Bottou, & K. Weinberger (Eds.), *Advances in neural information processing systems* (Vol. 25). Curran Associates, Inc. Retrieved from https://proceedings.neurips.cc/paper/2012/file/c399862d3b9d6b76c8436e924a68c45b-Paper.pdf

Kunkel, K. E., & Champion, S. M. (2019). An Assessment of Rainfall from Hurricanes Harvey and Florence Relative to Other Extremely Wet Storms in the United States. *Geophysical Research Letters*, *46*(22), 13500-13506. Retrieved from https://agupubs.onlinelibrary.wiley.com/doi/abs/10.1029/2019GL085034 doi: https://doi.org/10.1029/2019GL085034

Kunkel, K. E., Easterling, D. R., Kristovich, D. A. R., Gleason, B., Stoecker, L., & Smith, R. (2012). Meteorological Causes of the Secular Variations in Observed Extreme Precipitation Events for the Conterminous United States. *Journal of Hydrometeorology*, *13*(3), 1131 - 1141. Retrieved from https://journals.ametsoc.org/view/journals/hydr/13/3/jhm-d-11-0108_1.xml doi: 10.1175/JHM-D-11-0108.1

Lagerquist, R., Allen, J. T., & McGovern, A. (2020). Climatology and Variability of Warm and Cold Fronts over North America from 1979 to 2018. *Journal of Climate*, *33*(15), 6531 - 6554. Retrieved from https://journals.ametsoc.org/view/journals/clim/33/15/jcliD190680.xml doi: 10.1175/JCLI-D-19-0680.1

Lagerquist, R., McGovern, A., & II, D. J. G. (2019). Deep Learning for Spatially Explicit Prediction of Synoptic-Scale Fronts. *Weather and Forecasting*, *34*(4), 1137 - 1160. Retrieved from https://journals.ametsoc.org/view/journals/wefo/34/4/waf-d-18-0183_1.xml doi: 10.1175/WAF-D-18-0183.1

Lawrence, D. M., Oleson, K. W., Flanner, M. G., Thornton, P. E., Swenson, S. C., Lawrence, P. J., ... Slater, A. G. (2011). Parameterization improvements and functional and structural advances in Version 4 of the Community Land Model. *Journal of Advances in Modeling Earth Systems*, *3*(1). Retrieved from https://agupubs.onlinelibrary.wiley.com/doi/abs/10.1029/2011MS00045 doi: https://doi.org/10.1029/2011MS00045

LeCun, Y., Bengio, Y., & Hinton, G. (2015). Deep learning. *Nature*, *521*(7553), 436–444. Retrieved from https://doi.org/10.1038/nature14539 doi: 10.1038/nature14539

Leung, L. R., Boos, W. R., Catto, J. L., DeMott, C. A., Martin, G. M., Neelin, J. D., ... Zhou, Y. (2022). Exploratory Precipitation Metrics: Spatiotemporal Characteristics, Process-Oriented, and Phenomena-Based. *Journal of Climate*, *35*(12), 3659 - 3686. Retrieved from https://journals.ametsoc.org/view/journals/clim/35/12/JCLI-D-21-0590.1.xml doi: 10.1175/JCLI-D-21-0590.1

Liu, Y., Racah, E., Prabhat, Correa, J., Khosrowshahi, A., Lavers, D., ... Collins, W. (2016). *Application of Deep Convolutional Neural Networks for Detecting Extreme Weather in Climate Datasets.* arXiv. Retrieved from https://arxiv.org/abs/1605.01156 doi: 10.48550/ARXIV.1605.01156

Meehl, G. A., Washington, W. M., Arblaster, J. M., Hu, A., Teng, H., Kay, J. E., ... Strand, W. G. (2013). Climate Change Projections in CESM1(CAM5) Compared to CCSM4. *Journal of Climate*, *26*(17), 6287 - 6308. Retrieved from https://journals.ametsoc.org/view/journals/clim/26/17/jcli-d-12-00572.1.xml doi: 10.1175/JCLI-D-12-00572.1

Meehl, G. A., Yang, D., Arblaster, J. M., Bates, S. C., Rosenbloom, N., Neale, R., . . . Danabasoglu, G. (2019). Effects of Model Resolution, Physics, and Coupling on Southern Hemisphere Storm Tracks in CESM1.3. *Geophysical Research Letters*, *46*(21), 12408-12416. Retrieved from https://agupubs.onlinelibrary.wiley.com/doi/abs/10.1029/2019GL084057 doi: https://doi.org/10.1029/2019GL084057

Molina, M. J., Gagne, D. J., & Prein, A. F. (2021). A Benchmark to Test Generalization Capabilities of Deep Learning Methods to Classify Severe Convective Storms in a Changing Climate. *Earth and Space Science*, *8*(9), e2020EA001490. Retrieved from https://agupubs.onlinelibrary.wiley.com/doi/abs/10.1029/2020EA001490 doi: https://doi.org/10.1029/2020EA001490

National Weather Service. (2019, April). *National Weather Service Coded Surface Bulletins, 2003-* [dataset]. Zenodo. Retrieved from https://doi.org/10.5281/zenodo.2642801 doi: 10.5281/zenodo.2642801

Newman, M., & Sardeshmukh, P. D. (1998). The Impact of the Annual Cycle on the North Pacific/North American Response to Remote Low-Frequency Forcing. *Journal of the Atmospheric Sciences*, *55*(8), 1336 - 1353. Retrieved from https://journals.ametsoc.org/view/journals/atsc/55/8/1520-0469_1998_055_1336_tiotac_2.0.co_2.xml doi: 10.1175/1520-0469(1998)055⟨1336:TIOTAC⟩2.0.CO;2

Osman, M. B., Coats, S., Das, S. B., McConnell, J. R., & Chellman, N. (2021). North Atlantic jet stream projections in the context of the past 1,250 years. *Proceedings of the National Academy of Sciences*, *118*(38), e2104105118. Retrieved from https://www.pnas.org/doi/abs/10.1073/pnas.2104105118 doi: 10.1073/pnas.2104105118

Parfitt, R., Czaja, A., & Seo, H. (2017). A simple diagnostic for the detection of atmospheric fronts. *Geophysical Research Letters*, *44*(9), 4351-4358. Retrieved from https://agupubs.onlinelibrary.wiley.com/doi/abs/10.1002/2017GL073662 doi: https://doi.org/10.1002/2017GL073662

Park, S., Bretherton, C. S., & Rasch, P. J. (2014). Integrating Cloud Processes in the Community Atmosphere Model, Version 5. *Journal of Climate*, *27*(18), 6821 - 6856. Retrieved from https://journals.ametsoc.org/view/journals/clim/27/18/jcli-d-14-00087.1.xml doi: 10.1175/JCLI-D-14-00087.1

Pendergrass, A. G. (2018). What precipitation is extreme? *Science*, *360*(6393), 1072-1073. Retrieved from https://www.science.org/doi/abs/10.1126/science.aat1871 doi: 10.1126/science.aat1871

Pepler, A. S., Dowdy, A. J., & Hope, P. (2021). The differing role of weather systems in southern Australian rainfall between 1979–1996 and 1997–2015. *Climate Dynamics*, *56*(7), 2289–2302. Retrieved from https://doi.org/10.1007/s00382-020-05588-6 doi: 10.1007/s00382-020-05588-6

Pepler, A. S., Dowdy, A. J., van Rensch, P., Rudeva, I., Catto, J. L., & Hope, P. (2020). The contributions of fronts, lows and thunderstorms to southern Australian rainfall. *Climate Dynamics*, *55*(5), 1489–1505. Retrieved from https://doi.org/10.1007/s00382-020-05338-8 doi: 10.1007/s00382-020-05338-8

Priestley, M. D. K., & Catto, J. L. (2022). Improved Representation of Extratropical Cyclone Structure in HighResMIP Models. *Geophysical Research Letters*, *49*(5), e2021GL096708. Retrieved from https://agupubs.onlinelibrary.wiley.com/doi/abs/10.1029/2021GL096708 doi: https://doi.org/10.1029/2021GL096708

Riahi, K., Rao, S., Krey, V., Cho, C., Chirkov, V., Fischer, G., . . . Rafaj, P. (2011). RCP 8.5—A scenario of comparatively high greenhouse gas emissions. *Climatic Change*, *109*(1), 33. Retrieved from https://doi.org/10.1007/s10584-011

-0149-y doi: 10.1007/s10584-011-0149-y
Rudeva, I., & Simmonds, I. (2015). Variability and Trends of Global Atmospheric Frontal Activity and Links with Large-Scale Modes of Variability. *Journal of Climate*, *28*(8), 3311 - 3330. Retrieved from https://journals.ametsoc.org/view/journals/clim/28/8/jcli-d-14-00458.1.xml doi: 10.1175/JCLI-D-14-00458.1
Schär, C., Ban, N., Fischer, E. M., Rajczak, J., Schmidli, J., Frei, C., … Zwiers, F. W. (2016). Percentile indices for assessing changes in heavy precipitation events. *Climatic Change*, *137*(1), 201–216. Retrieved from https://doi.org/10.1007/s10584-016-1669-2 doi: 10.1007/s10584-016-1669-2
Schemm, S., Rudeva, I., & Simmonds, I. (2015). Extratropical fronts in the lower troposphere–global perspectives obtained from two automated methods. *Quarterly Journal of the Royal Meteorological Society*, *141*(690), 1686-1698. Retrieved from https://rmets.onlinelibrary.wiley.com/doi/abs/10.1002/qj.2471 doi: https://doi.org/10.1002/qj.2471
Schemm, S., Sprenger, M., Martius, O., Wernli, H., & Zimmer, M. (2017). Increase in the number of extremely strong fronts over Europe? A study based on ERA-Interim reanalysis (1979–2014). *Geophysical Research Letters*, *44*(1), 553-561. Retrieved from https://agupubs.onlinelibrary.wiley.com/doi/abs/10.1002/2016GL071451 doi: https://doi.org/10.1002/2016GL071451
Schemm, S., Sprenger, M., & Wernli, H. (2018). When during Their Life Cycle Are Extratropical Cyclones Attended by Fronts? *Bulletin of the American Meteorological Society*, *99*(1), 149 - 165. Retrieved from https://journals.ametsoc.org/view/journals/bams/99/1/bams-d-16-0261.1.xml doi: 10.1175/BAMS-D-16-0261.1
Shepherd, T. G. (2014). Atmospheric circulation as a source of uncertainty in climate change projections. *Nature Geoscience*, *7*(10), 703–708. Retrieved from https://doi.org/10.1038/ngeo2253 doi: 10.1038/ngeo2253
Sillmann, J., Kharin, V. V., Zhang, X., Zwiers, F. W., & Bronaugh, D. (2013). Climate extremes indices in the CMIP5 multimodel ensemble: Part 1. Model evaluation in the present climate. *Journal of Geophysical Research: Atmospheres*, *118*(4), 1716-1733. Retrieved from https://agupubs.onlinelibrary.wiley.com/doi/abs/10.1002/jgrd.50203 doi: https://doi.org/10.1002/jgrd.50203
Sillmann, J., Kharin, V. V., Zwiers, F. W., Zhang, X., & Bronaugh, D. (2013). Climate extremes indices in the CMIP5 multimodel ensemble: Part 2. Future climate projections. *Journal of Geophysical Research: Atmospheres*, *118*(6), 2473-2493. Retrieved from https://agupubs.onlinelibrary.wiley.com/doi/abs/10.1002/jgrd.50188 doi: https://doi.org/10.1002/jgrd.50188
Simmonds, I., Keay, K., & Bye, J. A. T. (2012). Identification and Climatology of Southern Hemisphere Mobile Fronts in a Modern Reanalysis. *Journal of Climate*, *25*(6), 1945 - 1962. Retrieved from https://journals.ametsoc.org/view/journals/clim/25/6/jcli-d-11-00100.1.xml doi: 10.1175/JCLI-D-11-00100.1
Smith, R. D., Jones, P., Briegleb, B., Bryan, F., Danabasoglu, G., Dennis, J., … Hecht, M. (2010). *The Parallel Ocean Program (POP) reference manual* (Tech. Rep. No. LAUR-10-01853). Los Alamos National Laboratory.
Soster, F., & Parfitt, R. (2022). On Objective Identification of Atmospheric Fronts and Frontal Precipitation in Reanalysis Datasets. *Journal of Climate*, *35*(14), 4513 - 4534. Retrieved from https://journals.ametsoc.org/view/journals/clim/35/14/JCLI-D-21-0596.1.xml doi: 10.1175/JCLI-D-21-0596.1
Srivastava, A., Grotjahn, R., & Ullrich, P. A. (2020). Evaluation of historical CMIP6 model simulations of extreme precipitation over contiguous US regions. *Weather and Climate Extremes*, *29*, 100268. Retrieved from https://

www.sciencedirect.com/science/article/pii/S2212094719302464 doi: https://doi.org/10.1016/j.wace.2020.100268

Tebaldi, C., Hayhoe, K., Arblaster, J. M., & Meehl, G. A. (2006). Going to the Extremes. *Climatic Change*, *79*(3), 185–211. Retrieved from https://doi.org/10.1007/s10584-006-9051-4 doi: 10.1007/s10584-006-9051-4

Thomas, C. M., & Schultz, D. M. (2019a). Global Climatologies of Fronts, Airmass Boundaries, and Airstream Boundaries: Why the Definition of "Front" Matters. *Monthly Weather Review*, *147*(2), 691 - 717. Retrieved from https://journals.ametsoc.org/view/journals/mwre/147/2/mwr-d-18-0289.1.xml doi: 10.1175/MWR-D-18-0289.1

Thomas, C. M., & Schultz, D. M. (2019b). What are the Best Thermodynamic Quantity and Function to Define a Front in Gridded Model Output? *Bulletin of the American Meteorological Society*, *100*(5), 873 - 895. Retrieved from https://journals.ametsoc.org/view/journals/bams/100/5/bams-d-18-0137.1.xml doi: 10.1175/BAMS-D-18-0137.1

Utsumi, N., Kim, H., Kanae, S., & Oki, T. (2016). Which weather systems are projected to cause future changes in mean and extreme precipitation in CMIP5 simulations? *Journal of Geophysical Research: Atmospheres*, *121*(18), 10,522-10,537. Retrieved from https://agupubs.onlinelibrary.wiley.com/doi/abs/10.1002/2016JD024939 doi: https://doi.org/10.1002/2016JD024939

van Vuuren, D. P., Stehfest, E., den Elzen, M. G. J., Kram, T., van Vliet, J., Deetman, S., … van Ruijven, B. (2011). RCP2.6: exploring the possibility to keep global mean temperature increase below 2 °C. *Climatic Change*, *109*(1), 95. Retrieved from https://doi.org/10.1007/s10584-011-0152-3 doi: 10.1007/s10584-011-0152-3

Wehner, M. F., Reed, K. A., Li, F., Prabhat, Bacmeister, J., Chen, C.-T., … Jablonowski, C. (2014). The effect of horizontal resolution on simulation quality in the Community Atmospheric Model, CAM5.1. *Journal of Advances in Modeling Earth Systems*, *6*(4), 980-997. Retrieved from https://agupubs.onlinelibrary.wiley.com/doi/abs/10.1002/2013MS000276 doi: https://doi.org/10.1002/2013MS000276

Wong, K. Y., Yip, C. L., & Li, P. W. (2008). Automatic identification of weather systems from numerical weather prediction data using genetic algorithm. *Expert Systems with Applications*, *35*(1), 542-555. Retrieved from https://www.sciencedirect.com/science/article/pii/S0957417407003065 doi: https://doi.org/10.1016/j.eswa.2007.07.032

Yang, B., Qian, Y., Lin, G., Leung, R., & Zhang, Y. (2012). Some issues in uncertainty quantification and parameter tuning: a case study of convective parameterization scheme in the WRF regional climate model. *Atmospheric Chemistry and Physics*, *12*(5), 2409–2427. Retrieved from https://acp.copernicus.org/articles/12/2409/2012/ doi: 10.5194/acp-12-2409-2012

Zhang, X., Alexander, L., Hegerl, G. C., Jones, P., Tank, A. K., Peterson, T. C., … Zwiers, F. W. (2011). Indices for monitoring changes in extremes based on daily temperature and precipitation data. *WIREs Climate Change*, *2*(6), 851-870. Retrieved from https://wires.onlinelibrary.wiley.com/doi/abs/10.1002/wcc.147 doi: https://doi.org/10.1002/wcc.147

Supporting Information for "Machine learning-based detection of weather fronts and associated extreme precipitation in historical and future climates"

Katherine Dagon[1], John Truesdale[1], James C. Biard[2], Kenneth E. Kunkel[3],

Gerald A. Meehl[1], and Maria J. Molina[1]

[1]National Center for Atmospheric Research, Boulder, CO, USA

[2]ClimateAi, San Francisco, CA, USA

[3]North Carolina Institute for Climate Studies, North Carolina State University, Asheville, NC, USA

Contents of this file

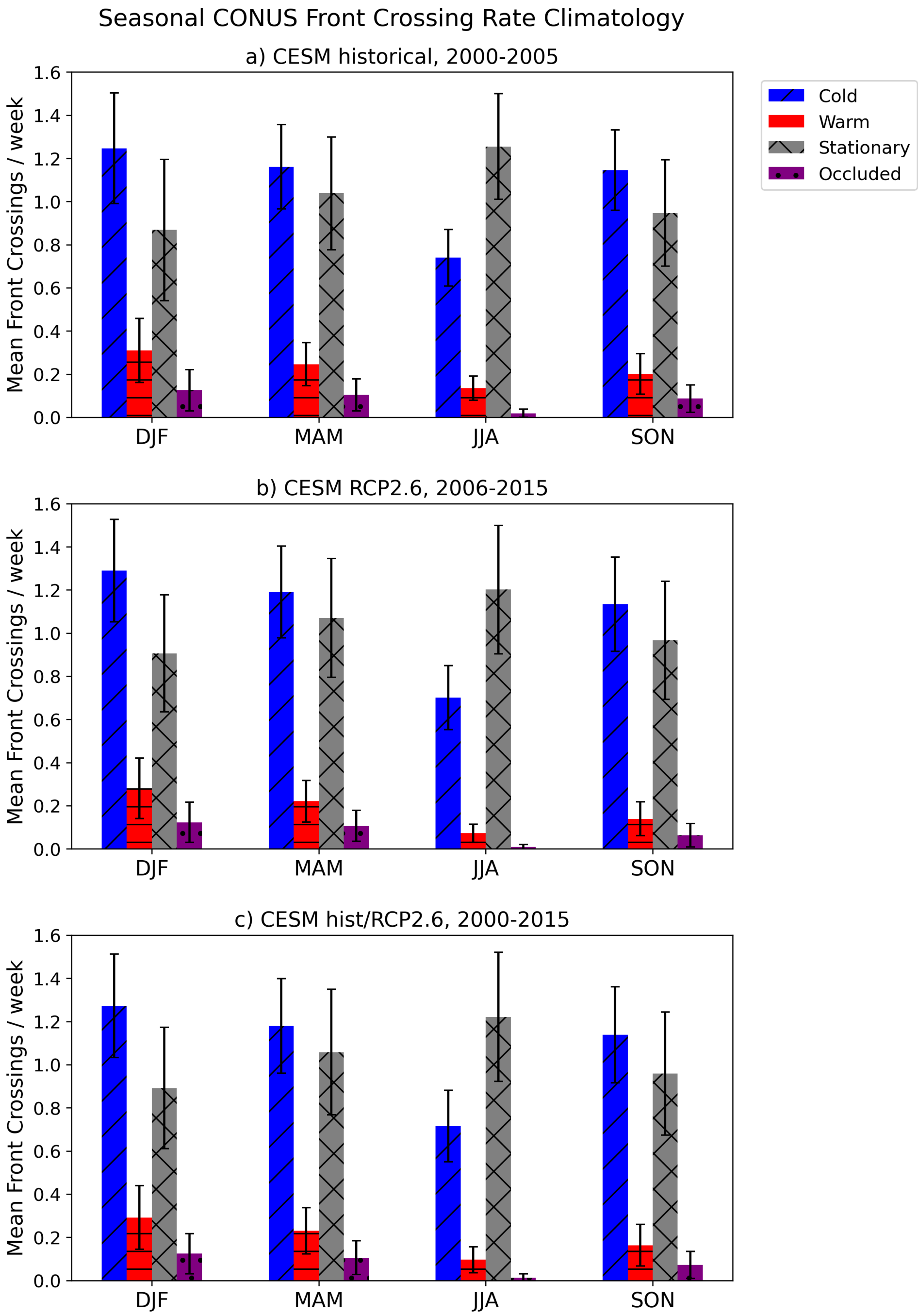

Figure S1. Seasonal CONUS averaged front crossing rate climatologies (fronts/week) for cold fronts in blue diagonal hatching, warm fronts in red horizontal hatching, stationary fronts in grey cross hatching, and occluded fronts in purple dotted hatching. a) CESM historical simulation, 2000-2005. b) CESM RCP2.6 simulation, 2006-2015. c) CESM combined historical/RCP2.6 climatology, 2000-2015. Error bars show plus or minus the standard deviation across years and front types for each simulation.

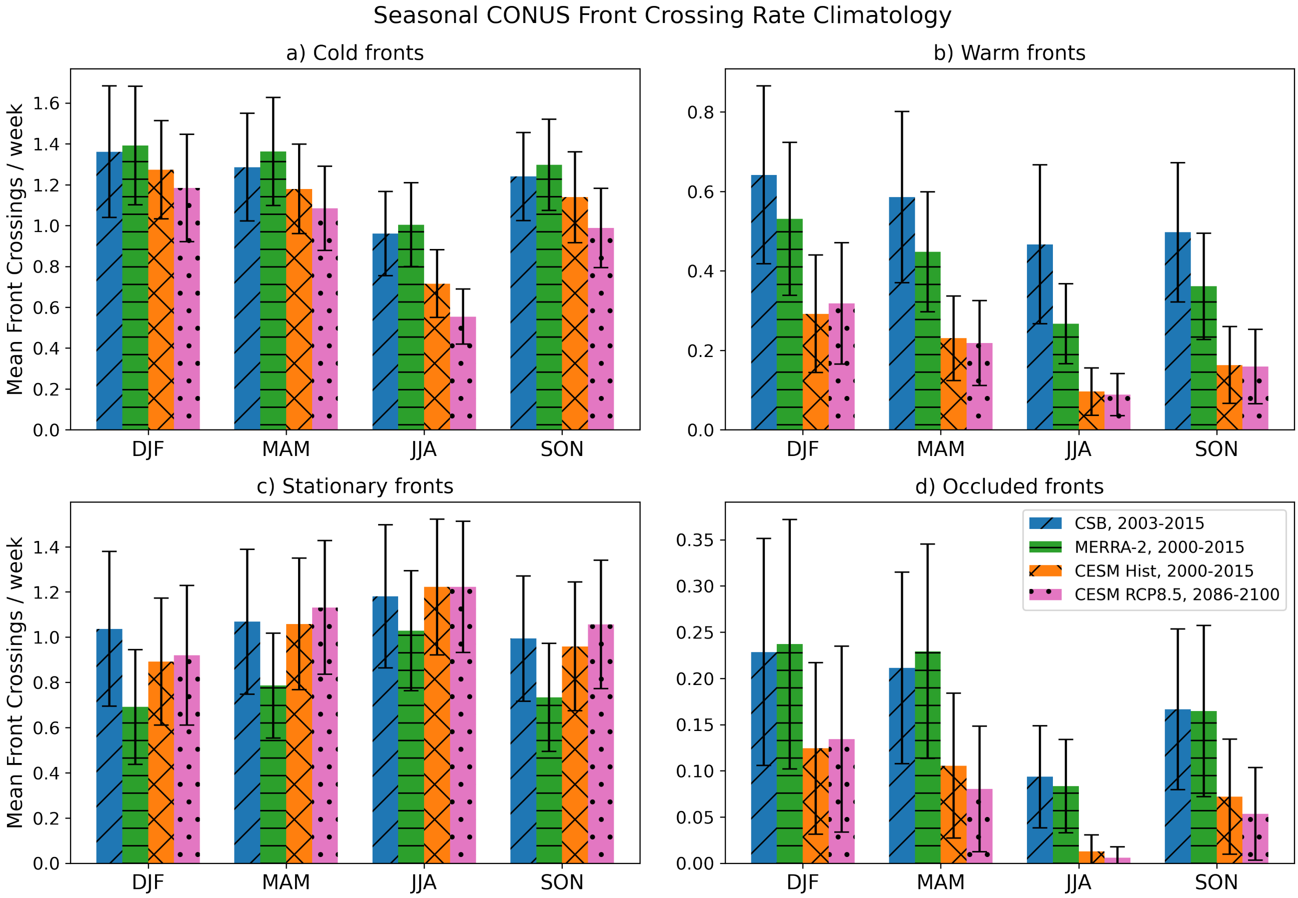

Figure S2. Seasonal CONUS averaged front crossing rate climatologies (fronts/week) for a) cold, b) warm, c) stationary, and d) occluded fronts. Coded Surface Bulletin (CSB) dataset (2003-2015) in blue diagonal hatching, MERRA-2 reanalysis dataset (2000-2015) in green horizontal hatching, CESM historical simulation (2000-2015) in orange cross hatching, and CESM RCP8.5 simulation (2086-2100) in pink dotted hatching. Error bars show plus or minus the standard deviation across years and front types for each simulation.

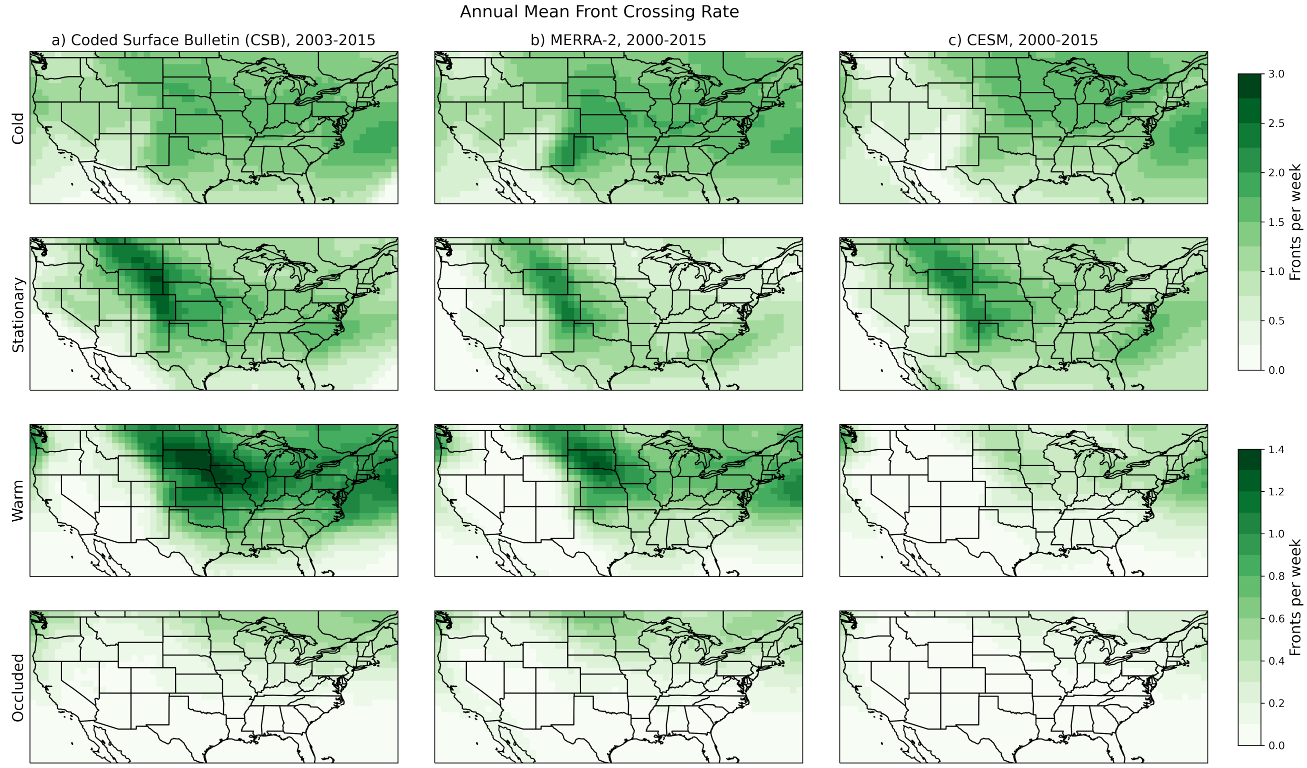

Figure S3. Annual mean front crossing rates (fronts/week) for four different front types in each row (cold, stationary, warm, and occluded fronts). a) Coded Surface Bulletin (CSB) dataset (2003-2015). b) MERRA-2 reanalysis dataset (2000-2015). c) CESM historical simulation (2000-2015). Note the differences in color scale for cold and stationary fronts (top rows) and warm and occluded fronts (bottom rows).

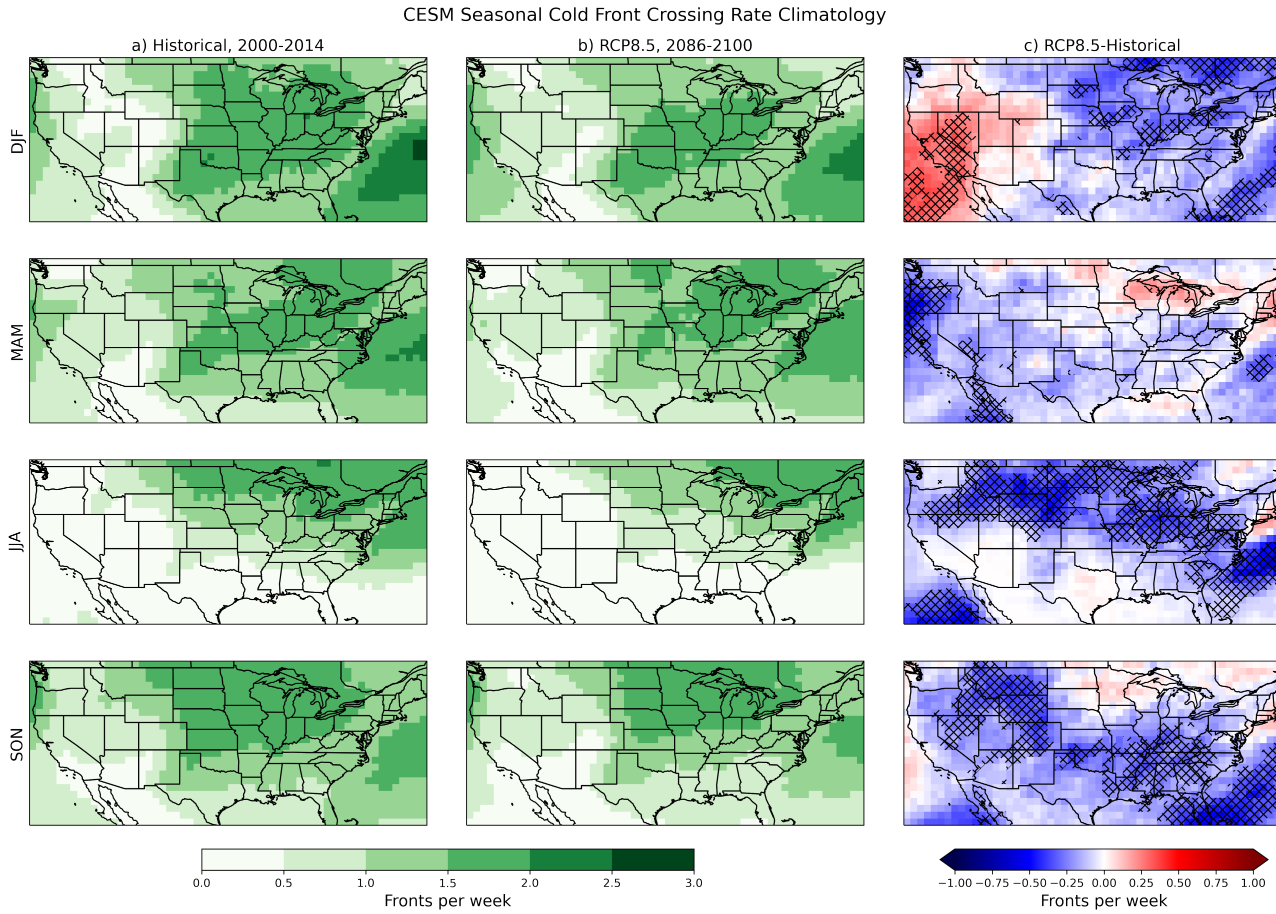

Figure S4. As in Figure 3, for cold fronts. Note the changes in color scale relative to Figure 3.

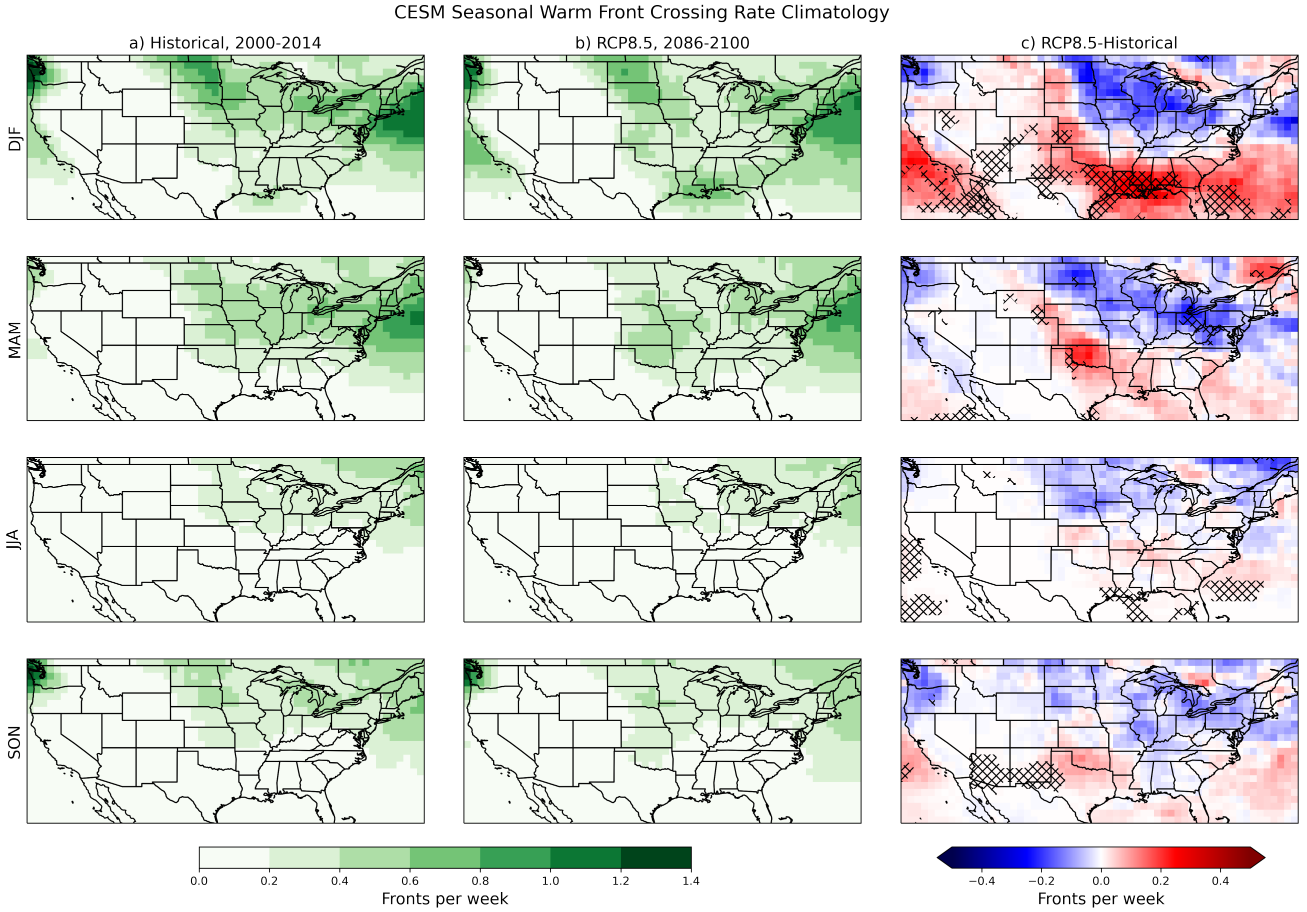

Figure S5. As in Figure 3, for warm fronts. Note the changes in color scale relative to Figure 3.

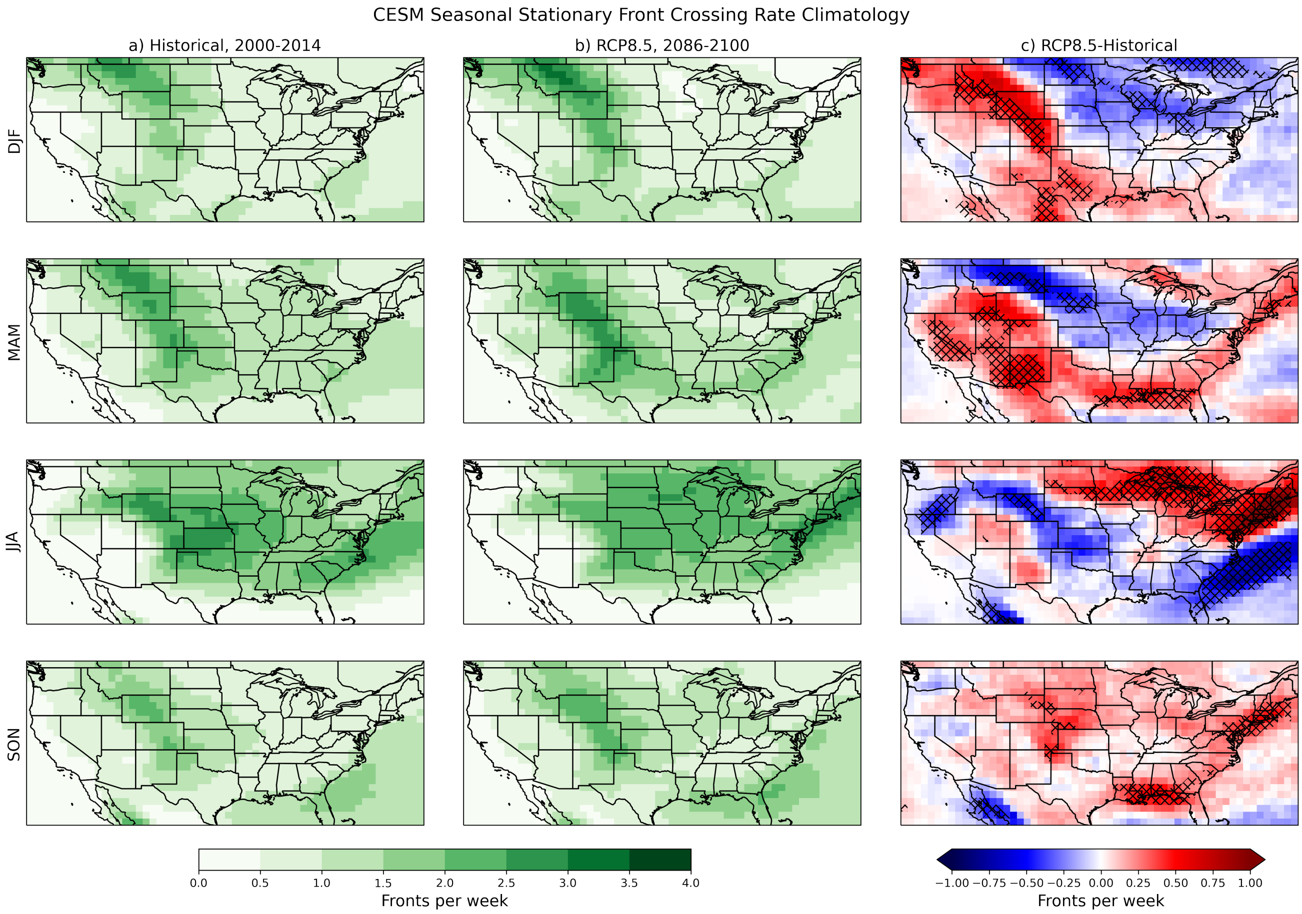

Figure S6. As in Figure 3, for stationary fronts.

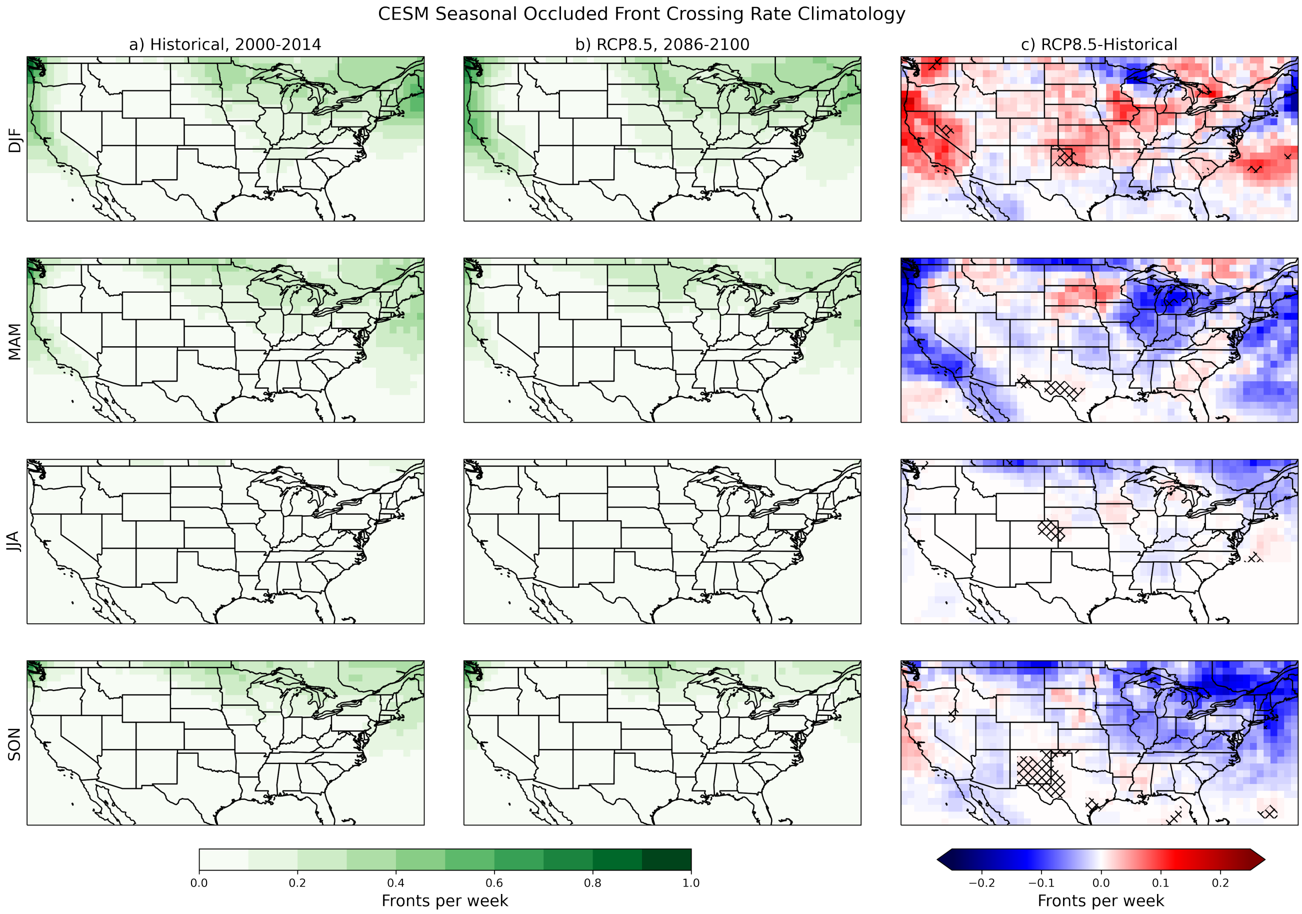

Figure S7. As in Figure 3, for occluded fronts. Note the changes in color scale relative to Figure 3.

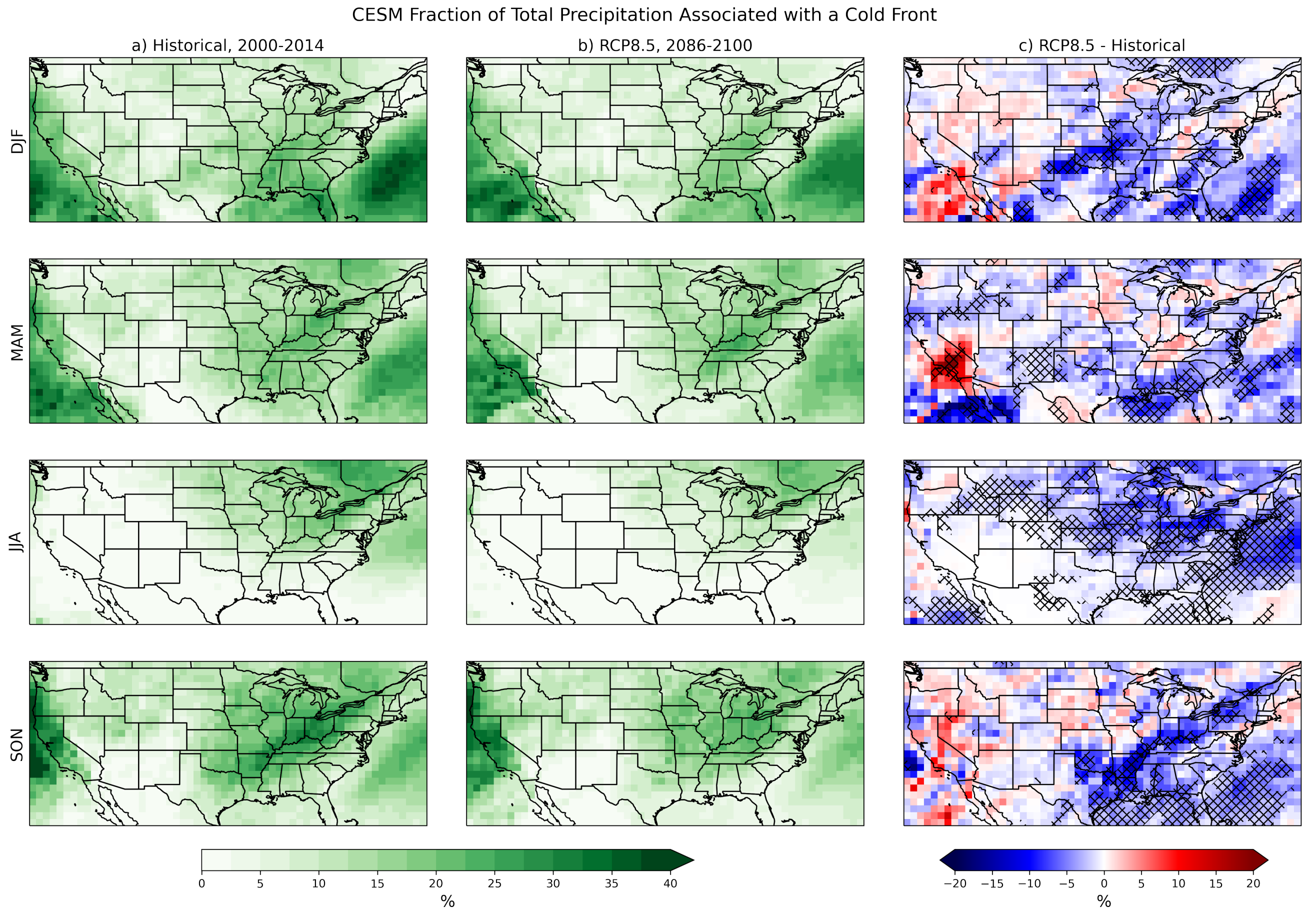

Figure S8. As in Figure 5, for cold fronts. Note the changes in color scale relative to Figure 5.

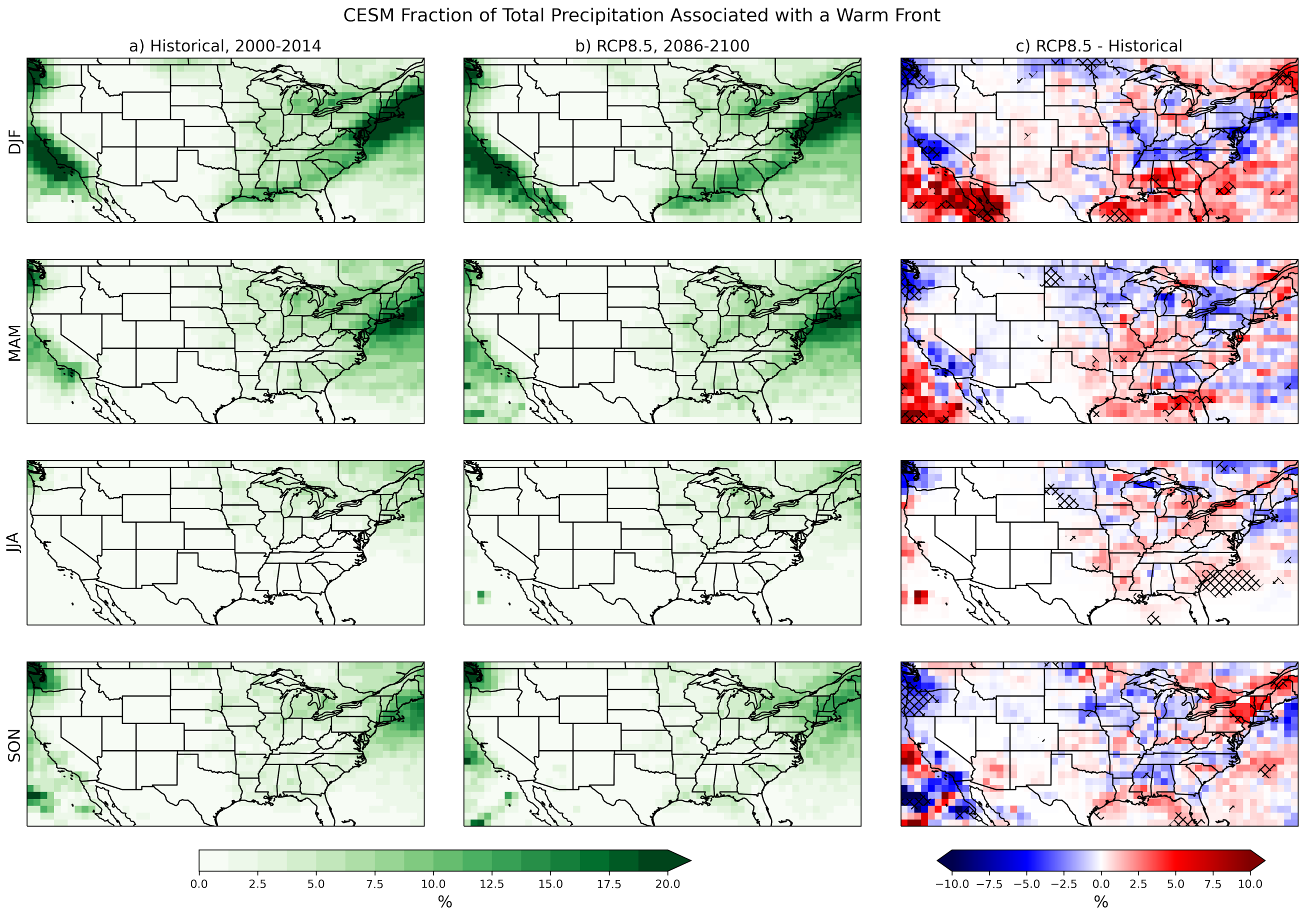

Figure S9. As in Figure 5, for warm fronts. Note the changes in color scale relative to Figure 5.

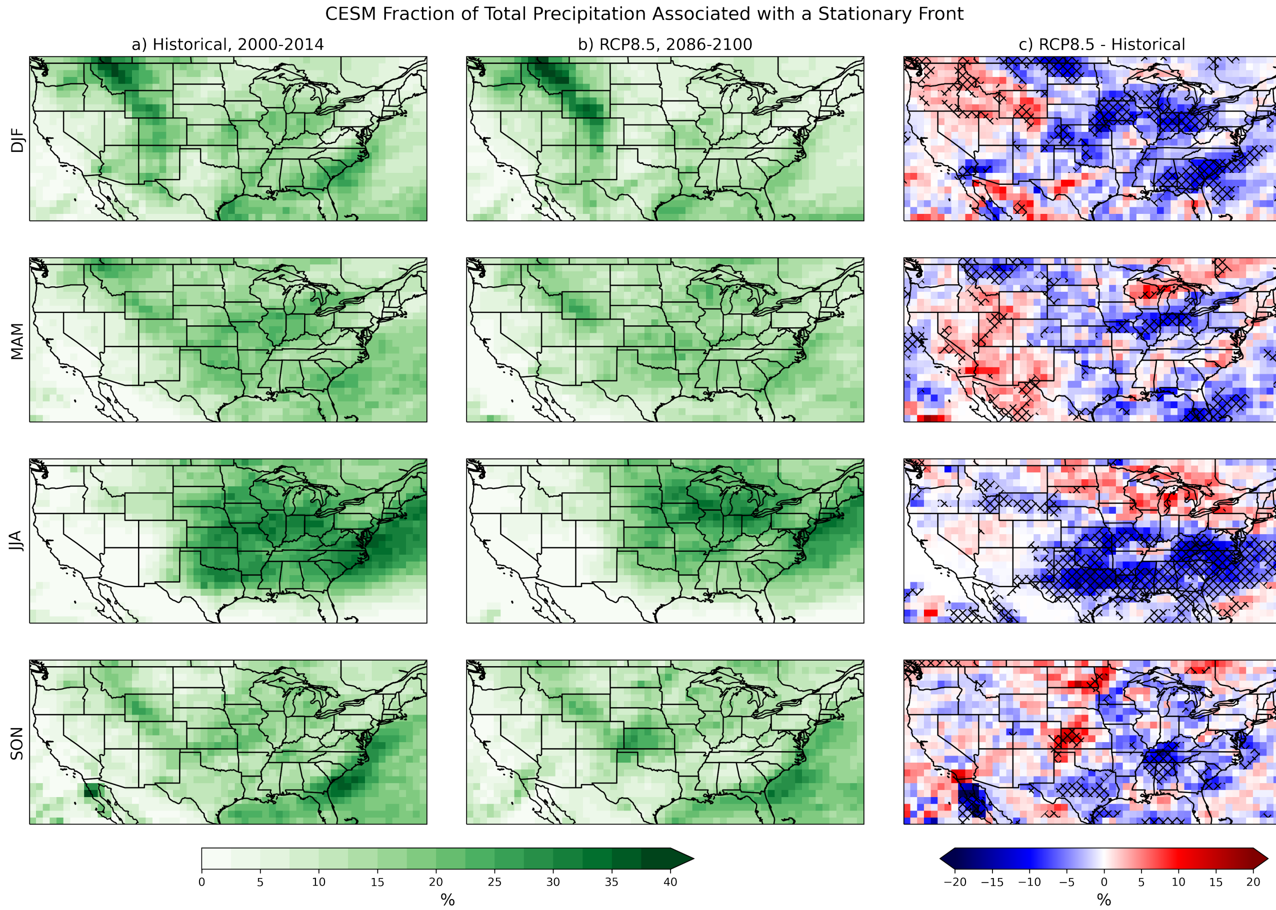

Figure S10. As in Figure 5, for stationary fronts. Note the changes in color scale relative to Figure 5.

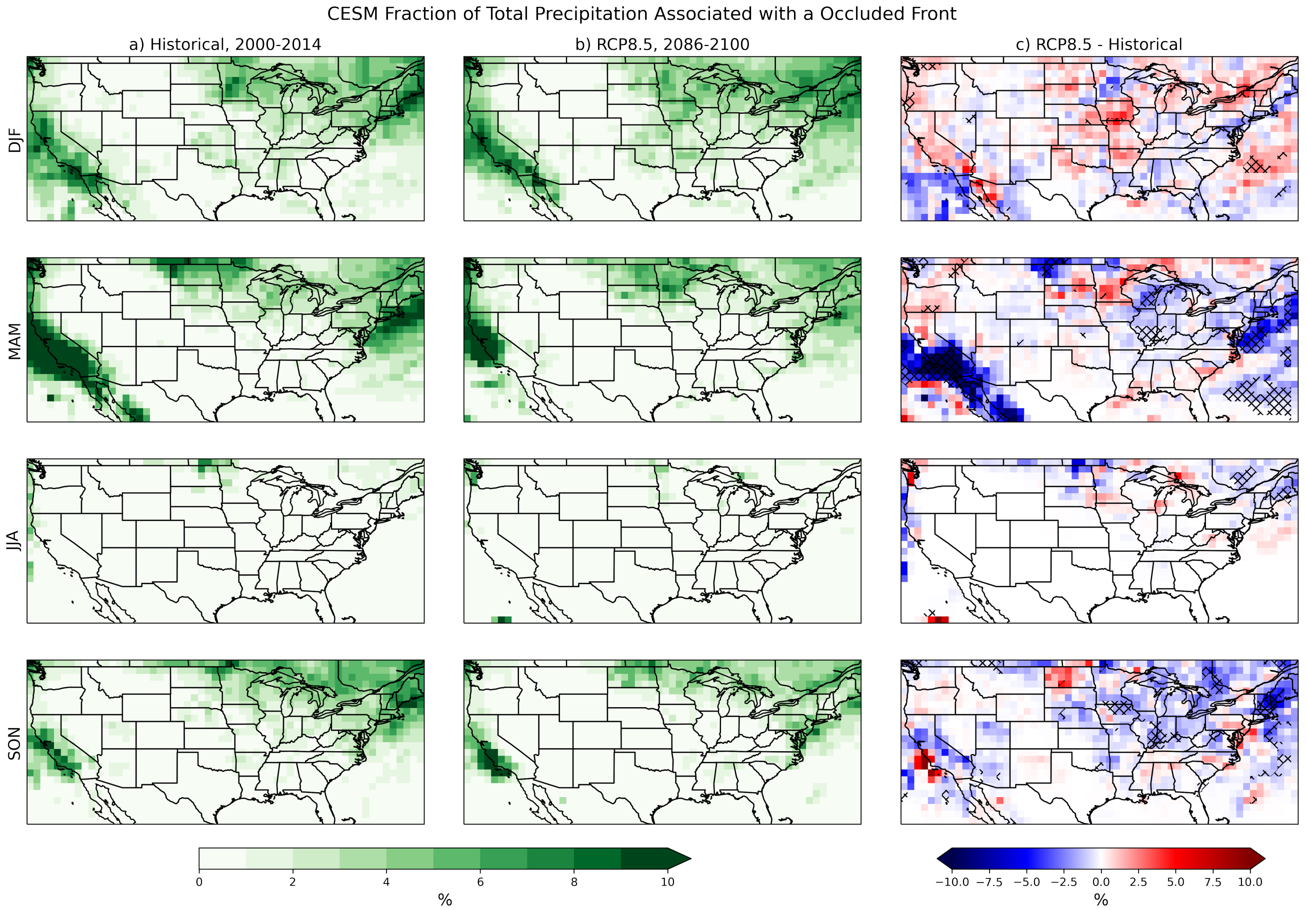

Figure S11. As in Figure 5, for occluded fronts. Note the changes in color scale relative to Figure 5.

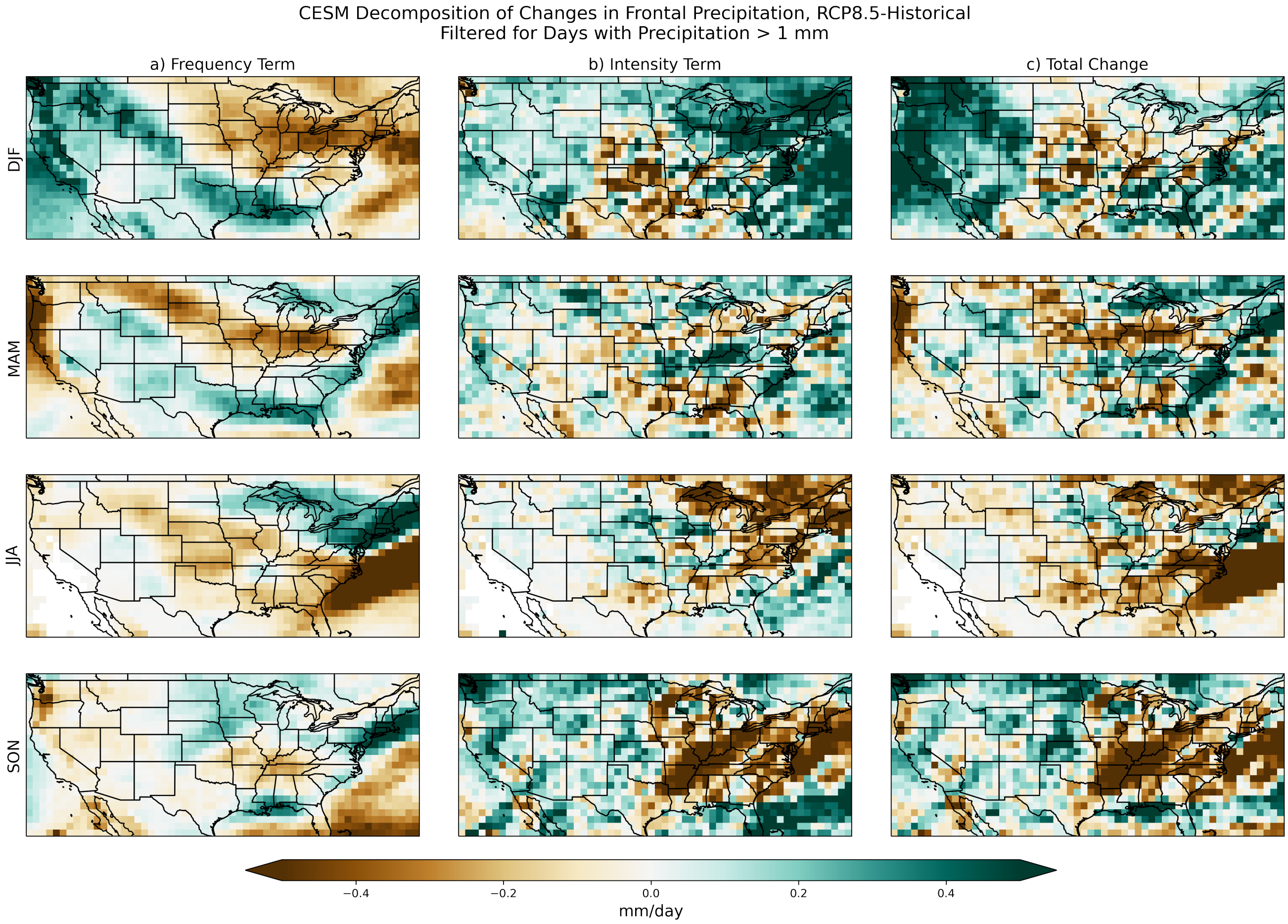

Figure S12. As in Figure 6, with the precipitation output filtered for days with precipitation greater than 1 mm.

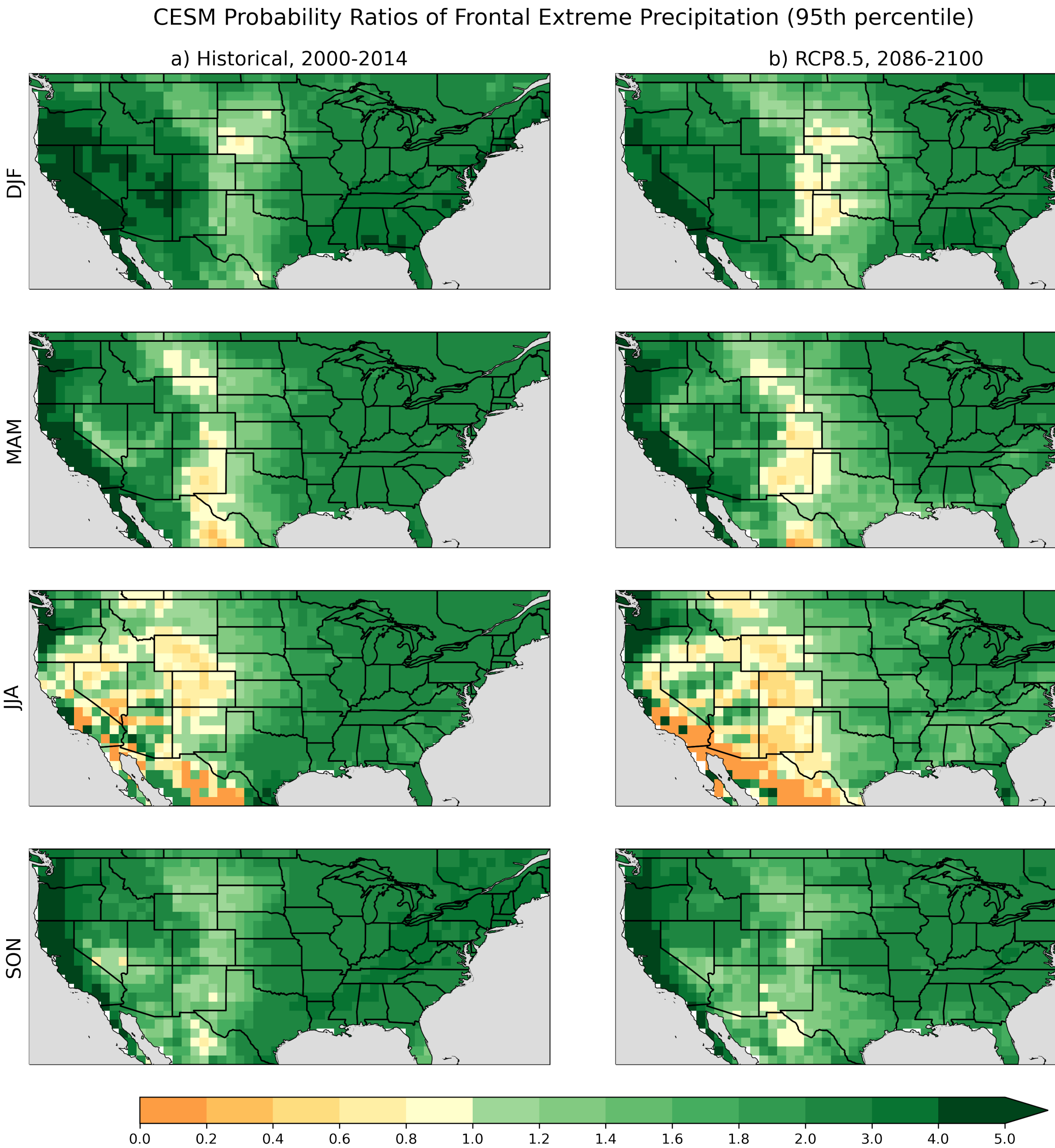

Figure S13. As in Figure 8, for 95th percentile precipitation.

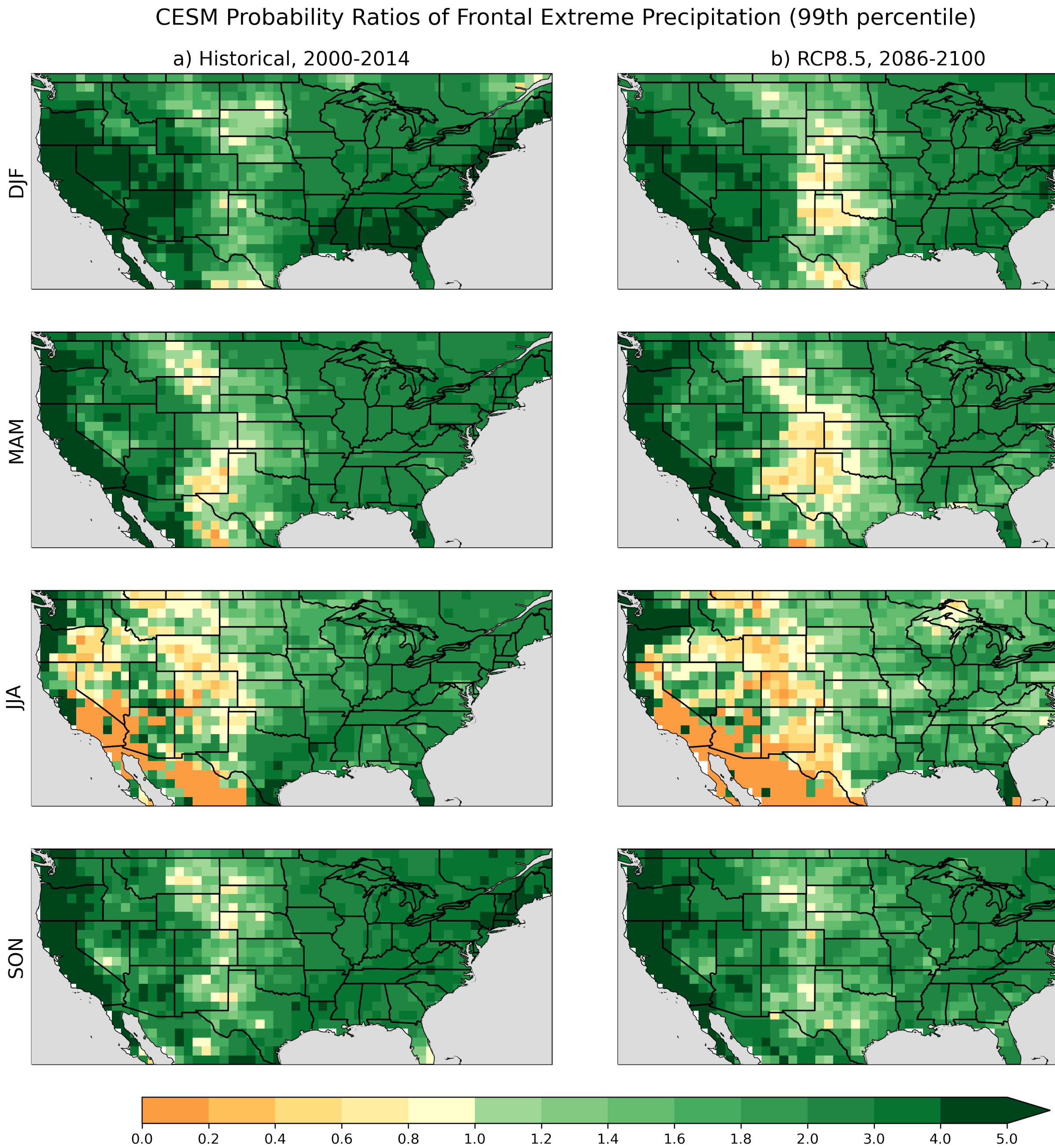

Figure S14. As in Figure 8, for 99th percentile precipitation.

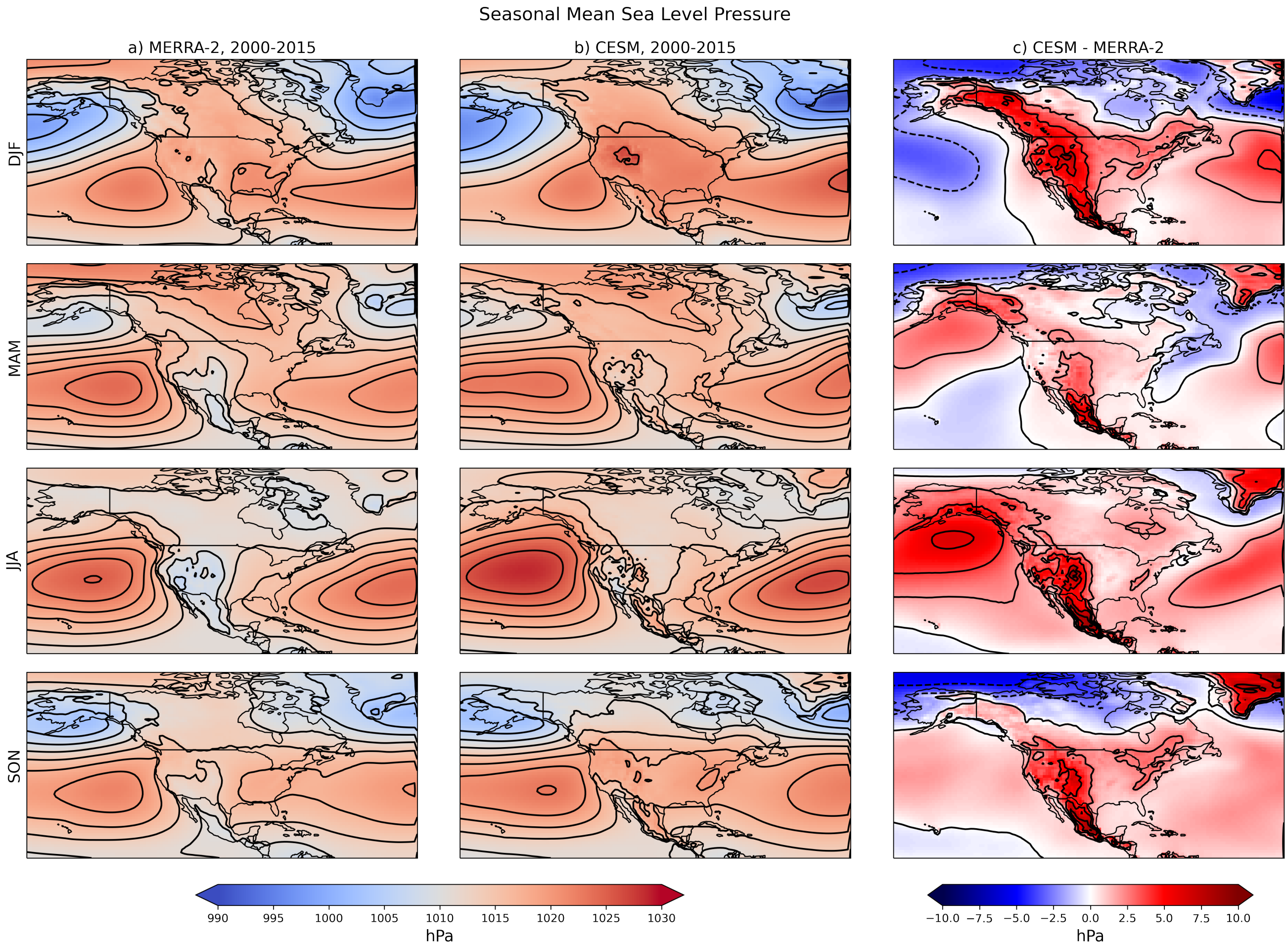

Figure S15. Seasonal mean climatology of sea level pressure (hPa) shown as contours (black lines, solid for positive values and dashed for negative values) and filled contours (shading). a) MERRA-2 reanalysis, and b) CESM output, both 2000-2015. c) The spatial difference for each season.